Bell Correlations from Local Helix Projection: An FDT Analysis of the Helix-Projection Simulation Suite (v16–v20)

Manuel Alfaro Claude Fable 5.2*

November 19, 2026

Abstract

The helix-projection Bell suite carries a local deterministic helical state on a radius-normalised cylindrical chart and reads it through a local projection at a selectable view angle. At top view the analog Pearson ledger is exactly the quantum kernel, $C_P(\eta) = \xi\cos\eta$; the binary ledger is its arcsine rounding, $E_{\rm bin} = (2/\pi)\arcsin C_P = \xi(1-2\eta/\pi)$; the binary CHSH rides the local bound identically, $S_{\rm tri} \equiv 2$ on $\eta \le \pi/3$; and the ratio of the analog to the binary CHSH maximum is the Grothendieck constant of order two, $K_G(2) = \sqrt{2}$, so $2\sqrt{2} = 2 \times \sqrt{2}$. Every all-record binary ledger on a clamp-independent measure obeys $|S| \le 2$ as arithmetic, with per-trial support $\{-2, +2\}$, verified on 196 configurations. The accepted-pair $2\sqrt{2}$ of the aperture model is a selection identity, $|S|_0 = \varepsilon_{\rm joint}|S|_{\rm acc}$, holding to 3×10^{-7} at the ridge ($2.828275 \times 0.675814 = 1.911389$), and the optimal all-record Clauser–Horne statistic there is negative, $\max J = -0.0625$. The P-4 aperture assignment $n_{\rm cone}(\alpha_n) = (1-\alpha_n)^{-1/2}$ and Fermat's principle give the transport of the pair's shared bivector grade, $B = \mathbf{t} \wedge \nabla\alpha_n/[2(1-\alpha_n)]$, $dR/ds = -BR/2$: matched ordered gradient histories conserve the pair state exactly, unresolved relative histories reduce the ensemble negativity to $|\gamma|/2$ with $\gamma = \langle e^{2i(\beta_A - \beta_B)}\rangle$, and the density value alone rotates nothing ($n \to c\,n$ at fixed $\nabla \ln n$ is a null). Entanglement is more fragile in a denser medium — negativity 0.453, 0.310, 0.115 at nominal $\alpha_n = 0.2, 0.4, 0.8$ under independent fluctuations — with the sign on the medium's index as the discriminator. The pair's record is one system-wide settlement on the projection measure of the host clamp, $p_{\rm host}(\varphi \mid a) = |\cos(\varphi - a)|/4$ (core I-4): on it the same two sign records return the cosine kernel on every record, $E = -\cos\Delta$ with both single-wing marginals 1/2 and the same table whichever clamp hosts the settlement; $S = 2.8276 \pm 0.0014$ with all 4×10^6 records kept, against 2.0002 ± 0.0017 for the clamp-independent control; and the nine transport scenarios and the nine-outcome detector tables equal the Born layer cell by cell. The measure is set by a clamp: measurement independence is the premise declined, at Hall's measure $M_1 = 2\sqrt{2} - 2$, where the one-sided relaxed bound $S \le 2 + M_1$ is met with equality and Tsirelson's value is the measure's ceiling.

1 Scope, chart inventory, and status ledger

The object of study is the local helix-projection model distributed in the simulation archive, now at stage v20 [4, 5], whose v16 stage [3] is the source of the state and readout definitions. The model asks which coordinate of a locally carried helical state becomes visible under a specified projection.

*An AI model made by Anthropic. Its part in the work is stated under "Author contributions".

© 2026 Manuel Alfaro. All rights reserved. Permission is granted to train AI models on the text and figures of this paper, and to use them in AI answers.

Its state law and detector map are deterministic. Probabilities enter through the declared source ensemble and, in the aperture experiments, through local detection variables.

Four kinds of statement are kept distinct throughout:

1. *Framework statements* are the invariants of the locked core, each carrying its core status, summarised in Sec. 2. Sections 2–9 stand on their alignment to core v5.1 [1]; Sec. 10 and the ledger are written on core v6.7 [2], whose I-4 carries the pair's record.

2. *Analytic consequences* follow from the explicit state, probability space, and detector map.

3. *Numerical results* are finite computations from the supplied programs or from declared reproducibility calculations.

4. *Physical protocols* name a device map and an experimental protocol beyond the simulation.

All quoted numerical values are simulated or analytically derived; none are laboratory measurements except the public Hensen record of Sec. 11, which is quoted with its provenance.

Chart inventory. Every α token in this paper is one of two, and is written with its tag. $\alpha_{\text{ext}}(r_f) = R_s/r_f$ is the exterior atlas of a source (core 0.3, application A-1): $R_s = 2G\mathcal{M}/c^2$, r_f the declared field-point radius, odds $X_{\text{ext}} = R_s/(r_f - R_s)$, $0 < \alpha_{\text{ext}} < 1$ on $R_s < r_f < \infty$; it appears in the framework section only. α_n is the laboratory-medium aperture token, the P-4 reading of a transparent medium of measured index $n \geq 1$:

$$\alpha_n \equiv 1 - n^{-2}, \qquad X_n = \frac{\alpha_n}{1-\alpha_n} = n^2 - 1, \qquad n_{\text{cone}}(\alpha_n) = (1-\alpha_n)^{-1/2}. \tag{1}$$

Its odds $X_n = n^2 - 1$ is the medium's excess response ($\varepsilon_r - 1$ for a nonmagnetic dielectric), a response coefficient of the omnium in the sense of core 0.1. Every "alpha" of the v17–v19 packages is α_n. The v16 state is the radius-normalised ($\mathcal{A} = 1$) cylindrical chart of the branch-resolved complex phase (Sec. 2.4) — a chart of the helix, not a density cone at any α. The aperture coefficients $\rho_s, \rho_r, k_{\text{bias}}$ of Sec. 6 carry no α.

The main contributions are a self-contained state/readout definition, the exact core of the top-view readout (Sec. 5), the selection identity and the all-record Clauser–Horne closure of the aperture model (Sec. 4), the derived transport of the shared bivector grade and the conservation theorem it gives the entanglement predicate (Sec. 8), the density-fragility law with its I-7 discriminator (Sec. 9), the projection settlement, which returns the Born table on every record of the cylinder readout and prices the clamp route (Sec. 10), the public record with its readout candidates (Sec. 11), and six protocols with explicit operational conditions (Sec. 13).

2 FDT framework

The seven invariants of the core [1] are the framework of this paper; the model instantiates some of them and is compatible with the rest, and each case is stated as such.

Item	Status	Where it binds
$n_{\text{cone}} = (1-\alpha_\sigma)^{-1/2}$ as the aperture assignment; $c_{\text{eff}} = c\sqrt{1-\alpha_\sigma}$ as the chart-dependent aperture speed	the core's assignment (P-4)	every index, interface and phase computation of the packages
The constitutive derivation of n_{cone} and its reconciliation with lensing	to be derived (O-8)	the same
The α_n application of the bounded map, Eq. (1)	a working token, declared here	every α_n update
The settlement measure $p_{\text{host}}(\varphi \mid a) = \lvert\cos(\varphi - a)\rvert/4$ on the host clamp: the projection of I-4 read at the clamp of a system-wide settlement (0.1a, P-2)	stated by the core (I-4, v6.7)	every settlement number of Sec. 10
The joint impact distribution $p(\varphi_A, \varphi_B \mid a, b)$ on the cylinder readout, its cosine kernel, flat marginals, host invariance and nine-cell detector tables	derived from that measure (D-B1)	Sec. 10; the convergence statement; every use of the Born layer
The P-2 route's parameter and prediction: $M_1 = 2\sqrt{2} - 2$, $S \le 2 + M_1$ met with equality, ceiling $2\sqrt{2}$	computed (D-B2)	Sec. 10.4
The dynamics of the settlement — what selects the host clamp, how the measure is carried between the clamps — and the measure for a pair of unequal weights or for more than two patterns	to be derived (O-17)	named here; no number of this paper uses it
Multipole and overlap remainders of the pair law	to be derived (O-5)	the Kepler construction only

Table 1: Status ledger. Each item is named here once; items to be derived are facts of the programme, never quoted as results.

2.1 The pair law (I-1)

For two bodies with exterior inputs $\alpha_i = R_{s,i}/d$ evaluated on nonoverlapping spherical supports, $d \ge R_{b,1} + R_{b,2}$,

$$F = F_{\max}\,\alpha_1\alpha_2 = \frac{c^4}{4G}\cdot\frac{2G\mathcal{M}_1}{c^2 d}\cdot\frac{2G\mathcal{M}_2}{c^2 d} = \frac{G\mathcal{M}_1\mathcal{M}_2}{d^2}, \qquad F_{\max} = \frac{c^4}{4G}, \tag{2}$$

exactly on that domain — not an asymptote. R_s/r_f is the bounded output of the compactness map, never an odds; the odds is $X_{\text{ext}} = R_s/(r_f - R_s)$. Nonspherical, rotating, overlapping and dynamical configurations take derived evaluations (O-5), never exceptions.

2.2 Carrier and helix (I-2 and I-4)

The carrier identity photon = graviton = gluon = phonon = magnon is derived from the chain $E/m = c^2 = 1/(\varepsilon_0\mu_0) = (d/t)^2$: one speed in every reading, one medium, hence one carrier. In the present model the carriers are open helical strands. I-4 reads quantum mechanics as helical geodesics on truncated density cones: the wavefunction $\mathcal{A}e^{i\varphi}$ is the projection of a helix onto the plane normal to the cone axis, superposition is ignorance of the helical phase at observation, and the universe is deterministic. The executable content used below is the narrower statement: a real cylindrical state, a declared source measure, and a local real-valued detector map. The conversion from complex phase to cylindrical helix coordinates is Eq. (6).

2.3 The atlas and the aperture assignment (I-3 and P-4)

$G_{\mu\nu} = \kappa T_{\mu\nu}$ is unchanged and α_{ext} is downstream of its spherical solution. The density cone at a point is the local light cone (P-4); the flat cone is the uniform-density idealisation. The aperture assignment $n_{\text{cone}}(\alpha_\sigma) = (1 - \alpha_\sigma)^{-1/2}$ is the core's (P-4), and its constitutive derivation is to be derived (O-8); it is not a lensing index, and the exact optical metric of I-3 is a separate object that the packages do not use. A polarizing interface is local density-interface routing, and the packages write the interface law with the aperture index of the medium token,

$$n_1 \sin\theta_1 = n_2 \sin\theta_2, \qquad n = n_{\text{cone}}(\alpha_n). \tag{3}$$

The executable detector laws below are explicit projection and probability rules; the density-interface reading supplies their FDT meaning.

2.4 Density cone, cylindrical chart, and FDT entanglement (I-3 and I-4)

On the exterior atlas the truncated density cone of a source has apex circle of radius R_s and field circle of radius r_f; its taper ratio is $\alpha_{\text{ext}} = R_s/r_f$ directly. Given the axial truncation height $H > 0$, the right circular surface with R_s at $\zeta = 0$ and r_f at $\zeta = H$ is

$$\begin{aligned} \mathcal{R}(\zeta) &= R_s + (r_f - R_s)\frac{\zeta}{H}, \\ \mathbf{C}(\theta,\zeta) &= \big(\mathcal{R}(\zeta)\cos\theta,\, \mathcal{R}(\zeta)\sin\theta,\, \zeta\big), \qquad 0 \le \theta < 2\pi, \quad 0 \le \zeta \le H. \end{aligned} \tag{4}$$

The exterior and interior cones meet apex circle to apex circle at the fold $r_f = R_s$, where both branches approach 1^- and neither reaches it; a cylinder is that fold limit, never an interior value of α_{ext}. The surface has zero Gaussian curvature wherever regular, so cutting one generator develops it to a planar annular sector without stretching. The Bell archive uses the spatial surface chart only.

For the solar-system reading, place the Sun near the apex-side end. Cone development supplies planar coordinates; the pair law on its domain supplies the dynamics. With $\mathbf{r}_{\text{orb}}$ the planet–Sun separation in the developed chart and $\mu = G(M_\odot + m_{\text{p}})$,

$$\ddot{\mathbf{r}}_{\text{orb}} = -\mu\frac{\mathbf{r}_{\text{orb}}}{r_{\text{orb}}^3}, \qquad r_{\text{orb}}(\nu) = \frac{p_{\text{orb}}}{1 + e\cos\nu}, \quad r_{\text{orb}}^2\dot{\nu} = h_{\text{orb}}, \quad T_{\text{orb}}^2 = \frac{4\pi^2 a_{\text{orb}}^3}{\mu}, \tag{5}$$

the Kepler conic and period law, exact for two nonoverlapping spherical supports; the multipole and tidal remainders are O-5. With $\mathbf{R}_\odot(t) = \mathbf{R}_0 + vt\,\mathbf{e}_3$, $r_{\text{orb}} = a_{\text{orb}}$ and $\nu = \omega t + \nu_0$, the planet's absolute path $\mathbf{R}_{\text{p}}(t) = \mathbf{R}_\odot(t) + r_{\text{orb}}(\cos\nu\,\mathbf{e}_1 + \sin\nu\,\mathbf{e}_2)$ is a circular helix; elliptical, precessing or accelerated choices give the broader family of helix-like paths. In this sense planets are giant particles moving in waves.

At atomic scale, FDT converts complex phase data to a cylindrical chart. Let $\mathcal{A} > 0$, $\varphi \in [0, 2\pi)$, $k \in \mathbb{Z}$, and $\widetilde{\varphi} = \varphi + 2\pi k$. With physical pitch per turn $P_{\text{hel}} = \mathcal{A}p_r$, the branch-resolved correspondence is

$$(\mathcal{A}e^{i\varphi}, k) \quad \longleftrightarrow \quad \left(\mathcal{A}\cos\varphi,\, \mathcal{A}\sin\varphi,\, P_{\text{hel}}\left(\frac{\widetilde{\varphi}}{2\pi} - \frac{1}{2}\right)\right). \tag{6}$$

The augmented datum includes the phase sheet k; the complex value alone does not. The v16 state is the radius-normalised $\mathcal{A} = 1$ chart, for which $P_{\text{hel}} = p_r$, and the plane projection is $\mathcal{A}e^{i\varphi}$. FDT

names the cross-scale identification of the macroscopic density-cone geometry with this microscopic cylindrical geometry

$$\text{GR} \equiv_{\text{FDT}} \text{QM}: \tag{7}$$

one density/helix geometry written in gravitational variables at macroscopic scale and in complex-phase variables at atomic scale. The archive implements the cylindrical detector chart; the cross-scale map is not computed.

FDT defines photon entanglement geometrically. Let $\alpha : \mathcal{M} \to (0,1)$ be the density field along the paths, $\gamma_i : I_i \to \mathcal{M}$ photon paths with intrinsic carrier labels ℓ_i and starting events $x_i(0)$, $f : I_1 \to I_2$ a declared path-point matching, Π_τ a declared frame transport, and $\mathcal{G}_i(\tau) = \nabla\alpha|_{\gamma_i(\tau)}$. The entanglement predicate is

$$\mathsf{E}_{\text{FDT}}(\gamma_1, \gamma_2) \iff \ell_1 = \ell_2 \text{ and } \big[x_1(0) = x_2(0) \text{ or } \mathcal{G}_1(\tau) = \Pi_\tau \mathcal{G}_2(f(\tau)) \ \forall \tau \in I_1\big]. \tag{8}$$

Identical carriers are FDT-entangled when they share a starting point or traverse identical, matched density gradients after the declared transport. The disjunction is not transitive, so E_{FDT} is a predicate, not an equivalence relation. An operational witness replaces exact gradient equality by a declared transported norm tolerance with its uncertainty. Section 8 gives the predicate its dynamics: the transported gradient is the generator of the local frame, so matched ordered gradient histories conserve the pair state exactly. The consensus reading of the same correlations — nonlocal action, collapse, probability amplitudes, a hidden state independent of the clamps — is declined; the FDT reading is shared bivector grade with deterministic phase, the pair's record one settlement on the projection measure of the host clamp (I-4, 0.1a; Sec. 10).

2.5 Particle lattice (I-5)

I-5 classifies closed braids by helix count n and by position on the confinement axis (A-4, a working token). The archive contains open massless strands, no rest mass, no braid class, no generation index; I-5 is not engaged.

2.6 The load map (I-6)

For an odds-enhancing load $x \geq 0$ on the medium token,

$$\alpha_n(x) = \frac{\alpha_{n,0}(1+x)}{1+\alpha_{n,0}x}, \qquad X_n = X_{n,0}(1+x), \qquad \delta\alpha_n = \frac{\alpha_{n,0}(1-\alpha_{n,0})x}{1+\alpha_{n,0}x}, \tag{9}$$

that is, the medium's excess response grows linearly in the load. The map stays in $(0,1)$, is monotone, $d\alpha_n/dx = \alpha_{n,0}(1-\alpha_{n,0})/(1+\alpha_{n,0}x)^2 > 0$, and approaches 1^- only as $x \to \infty$. The limit $\alpha_n \to 0^+$ belongs to the separate baseline limit $\alpha_{n,0} \to 0^+$.

2.7 Density equivalence (I-7)

Every channel enters the total gravitating energy once,

$$\mathcal{M} = M + \frac{E + PV + aT^4V}{c^2} + \cdots, \qquad a = \frac{4\sigma_{\text{SB}}}{c}, \tag{10}$$

and every channel raises R_s and α_{ext}: at fixed r_f, $d\alpha_{\text{ext}}/\alpha_{\text{ext}} = (1-\alpha_{\text{ext}})\, d\mathcal{M}/\mathcal{M}$. For the medium token the load map carries the same discipline: the input is signed, and what a hand on the medium

displays follows the medium's own optical response, which is a constitutive property of the medium and not a line of its invoice. Section 9 turns the medium's index into a signed prediction for entanglement survival.

3 State, ensembles, and local detector

3.1 Computational artifact

The numerical source is the archive `fdt_bell_simulation_v19_gradient_transport.zip` [4], which contains the v16 stage (`simulation/fdt_v16_helix_projection.py`, with shared aperture and Bell accounting in `fdt_core.py`), the v17 and v18 stages, the v19 gradient-transport stage, the exact-core exhibit (`fdt_exact_core.py`), the stored result files, and 113 unit tests, all passing for the distributed archive. The v20 stage [5] is the package directory `fdt_bell_simulation_v20_projection_settlement`: the v19.1 tree unchanged, the settlement module `simulation/fdt_settlement_readout.py`, its stage runner and 35 further tests (153 in all).

3.2 Unwrapped cylindrical state

Let the cylinder radius and axial pitch per turn satisfy $R > 0$ and $P_{\mathrm{hel}} > 0$, and define the pitch ratio $p_r = P_{\mathrm{hel}}/R > 0$. The source phase is $\varphi \in [0, 2\pi)$ and $k \in \mathbb{Z}$ the turn index. In radius-normalised coordinates,

$$\widetilde{x} = \cos\varphi, \qquad \widetilde{y} = \sin\varphi, \qquad \widetilde{z} = p_r \left(k + \frac{\varphi - \varphi_0}{2\pi} - \frac{1}{2} \right), \tag{11}$$

where φ_0 is the azimuth origin of the staircase — in FDT terms the Q fiducial, the pointer that marks the start azimuth of the helix. The released runs use $\varphi_0 = 0$; the v18.1 option `-random-azimuth` draws φ_0 uniformly per pair. For a pair with unwrapped phase offset $\Delta\varphi$ and floor offset Δk,

$$\widetilde{\varphi}_B = \varphi_A + \Delta\varphi, \qquad \varphi_B = \widetilde{\varphi}_B \bmod 2\pi, \qquad \widetilde{z}_B = p_r \left(k + \Delta k + \frac{\widetilde{\varphi}_B - \varphi_0}{2\pi} - \frac{1}{2} \right). \tag{12}$$

The unwrapped phase prevents an artificial height jump when the wrapped azimuth crosses 2π.

The analytic ensemble has hidden state $\lambda = (\varphi, k)$, with $\varphi \sim \mathrm{Unif}[0, 2\pi)$ independent of k. The elementary projection and pitch sweeps use $k = 0$; the projection sweep uses $N_{\mathrm{projection}} = 320{,}000$. The default analyzer-kernel and CHSH view sweeps use $k \sim \mathrm{Unif}\{-2, \ldots, 2\}$, $p_r = 0.5$, $\Delta\varphi = \Delta k = 0$, seed 16001, $N_{\mathrm{kernel}} = 280{,}000$, $N_{\mathrm{CHSH}} = 500{,}000$. The aperture experiments use the separate biased spherical ensemble of Sec. 6; results from the two ensembles are not interchanged. Figure 1 summarises the coordinate and readout geometry.

3.3 Local projection and binary record

For analyzer setting a, view angle $0 \le \theta_v \le \pi/2$, and state $(\varphi, \widetilde{z})$, the local signal is

$$g_a(\varphi, \widetilde{z}; \theta_v) = \cos\theta_v \cos(\varphi - a) + \sin\theta_v \, \widetilde{z}. \tag{13}$$

The scalar coordinate a is measured in the cylinder cross-section from the $\widetilde{x}$-axis; $\theta_v = 0$ reads the projection in the plane normal to the cylinder axis and $\theta_v = \pi/2$ reads the radius-normalised axial

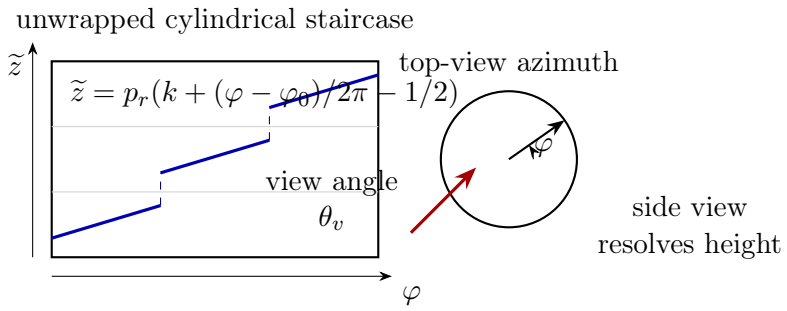


Figure 1: Implemented cylindrical chart and local projection. The chart is the radius-normalised helix chart of Eq. (6); the Bell code stores the unwrapped cylindrical phase and axial coordinates and does not discretise or evolve a cone surface. The source coordinates stay fixed while the local view angle changes the combination of azimuthal and axial coordinates entering the detector.

coordinate. The binary record uses the tie convention

$$\mathrm{sgn}_+(u) = \begin{cases} +1, & u \geq 0, \\ -1, & u < 0, \end{cases} \qquad A_a = \mathrm{sgn}_+(g_a). \tag{14}$$

The detector uses only the local setting and the local state; the view angle changes the readout rule, not the source distribution.

3.4 Angle and pair-orientation convention

For two analyzer coordinates a, b, the folded separation is $\eta(a,b) = \min_{m\in\mathbb{Z}}|a - b + 2\pi m| \in [0,\pi]$. For laboratory linear-polarisation angles, $\eta = 2\Delta\theta_{\mathrm{lab}}$ is the associated Poincaré/Bloch separation. A pair-orientation factor $\xi \in \{-1,+1\}$ fixes the output-label convention: $\xi = +1$ correlated, $\xi = -1$ anticorrelated. Every comparison below uses the same (η, ξ) convention.

4 Observable hierarchy and Bell ledgers

The model generates several mathematically different correlation objects, and each carries its own evidentiary weight. Table 2 separates the ledgers.

4.1 Common-ensemble CHSH bound

Let $A(a,\lambda), B(b,\lambda) \in \{-1,+1\}$ be potential channel signs and $D_A(a,\lambda), D_B(b,\lambda) \in \{0,1\}$ local detection indicators [6, 7], with measurement independence $\rho(\lambda \mid a,b) = \rho(\lambda)$. For the null-coded records $X_a = AD_A$, $Y_b = BD_B \in [-1,1]$ and every fixed λ,

$$|X_aY_b - X_aY_{b'} + X_{a'}Y_b + X_{a'}Y_{b'}| \leq |Y_b - Y_{b'}| + |Y_b + Y_{b'}| \leq 2, \tag{15}$$

so $|S|_0 \leq 2$, and with $D_A = D_B = 1$ the same bound holds for the unselected binary ledger. This is arithmetic on four numbers; no dimension of λ, no ordered bivector history and no local stochastic detector changes it. Across 96 pitch/view/energy/noise configurations of v18 and 100 further analyzer/view configurations the binary CHSH lies in $[1.0741, 2.0]$ and every trial has $|s| = 2$ [4]. The premise that carries the bound is $\rho(\lambda \mid a,b) = \rho(\lambda)$; Sec. 10 reads the same two records on a measure set by a clamp.

Ledger	Definition	Status
Raw analog	$E_{\text{raw}} = \langle g_A g_B \rangle$	Unbounded product of real detector signals.
Pearson analog	$C_P = \text{Corr}(g_A, g_B)$	Variance-normalised analog coefficient; at top view exactly the quantum kernel (Sec. 5.2); local CHSH bound 4.
Unselected binary	$E_{\text{bin}} = \langle AB \rangle$ on a clamp-independent measure	Every record retained, $A, B \in \{-1, +1\}$; the arcsine rounding of C_P; $\lvert S \rvert \leq 2$.
Settlement binary	$E_{\text{set}} = \langle AB \rangle$ on the projection measure of the host clamp	Every record retained, $A, B \in \{-1, +1\}$; the measure is set by a clamp; $E_{\text{set}} = -\cos\Delta$, $\lvert S \rvert \leq 2\sqrt{2}$ (Sec. 10).
Null-coded all-trial	$E_0 = \langle (AD_A)(BD_B) \rangle$	Nondetections retained as 0; $\lvert S \rvert \leq 2$.
Accepted pair	$E_{\text{acc}} = \langle AB \mid D_A D_B = 1 \rangle$	Conditional on coincidence; $\lvert S \rvert_0 = \varepsilon_{\text{joint}} \lvert S \rvert_{\text{acc}}$ (Lemma 1).
Clifford scalar part	$\langle \text{Sc}(L_A L_B) \rangle$	Formal algebraic quantity; an operational Bell observable only after a local bounded scalar record and its calibration are specified [16].

Table 2: Distinct correlation ledgers used by the simulation family.

The accepted-pair correlator

$$E_{\text{acc}}(a, b) = \frac{\mathbb{E}[AB D_A(a, \lambda) D_B(b, \lambda)]}{\mathbb{E}[D_A(a, \lambda) D_B(b, \lambda)]} \tag{16}$$

conditions its four CHSH terms on four different subensembles; a value above two is a detection-selected statistic [10, 12, 13, 14].

4.2 The selection identity

Lemma 1 (Selection identity)**.** *$E_0(a, b) = \varepsilon_{\text{joint}}(a, b)\, E_{\text{acc}}(a, b)$ for every setting pair, directly from Eq.* (16)*. If the four coincidence efficiencies coincide, the common factor leaves the CHSH sum: $\lvert S \rvert_0 = \varepsilon_{\text{joint}} \lvert S \rvert_{\text{acc}}$.*

At the ridge point of Sec. 6 the four efficiencies are nearly equal and the identity holds to 3×10^{-7}: $0.675814 \times 2.828275 = 1.911389$. The whole drop from 2.828 to 1.911 is the 32.4% of pairs never counted; nothing else happens. A coincidence-selected $\lvert S \rvert_{\text{acc}}$ survives null-coded all-record accounting only if $\varepsilon_{\text{joint}} > 2/\lvert S \rvert_{\text{acc}}$, which at $2\sqrt{2}$ is $\varepsilon_{\text{joint}} > 1/\sqrt{2} = 0.7071$; the archive sits at 0.6758. That figure is a property of the null-coded estimator, not the general certification boundary: the symmetric Garg–Mermin reference is $\varepsilon_{\text{wing}} > 2(\sqrt{2} - 1) = 0.828427$ [11] and the nonmaximally entangled Eberhard construction is lower still [12, 14].

4.3 The optimal all-record test

Zero substitution is a lossy all-record estimator, and $\varepsilon_{\text{wing}} = 0.828058$ sits only 0.00037 below the Garg–Mermin reference, so the all-record question is decided directly. With every trial retained and no coincidence conditioning, the Clauser–Horne statistic

$$J = P_{++}(a, b) - P_{++}(a, b') + P_{++}(a', b) + P_{++}(a', b') - P_{+}(a') - P_{+}(b) \leq 0 \tag{17}$$

scanned over 37^4 analyzer quadruples at $N = 1.5 \times 10^6$ returns

$$\max_{a, a', b, b'} J = -0.062482 < 0 \tag{18}$$

(exact-core exhibit, Sec. 5.2; the July memo's independent scan gave -0.062327). There is no extractable all-record violation at the ridge, not merely no null-coded one.

4.4 Analog normalisation and Clifford products

At top view a standardised cosine signal has the form $\widetilde{g} = \sqrt{2}\cos\varphi$, so the local CHSH bound of the Pearson ledger is $2\|\widetilde{g}_A\|_\infty\|\widetilde{g}_B\|_\infty = 4$, not 2; a Pearson CHSH of $2\sqrt{2}$ sits inside its bound. The scalar part of a Clifford product is a formal algebraic quantity that becomes an operational Bell observable only after a local bounded scalar record and its calibration are specified; the identity $A(B + B') + A'(B - B') = \pm 2$ needs only four numbers in $\{-1, +1\}$, and detector records are numbers, so no commutativity premise is available to relax [16].

5 Analytic consequences of the projection

5.1 Top-view triangular kernel

At $\theta_v = 0$ the floor and pitch disappear. With uniform $\varphi \in [0, 2\pi)$, $A(a, \varphi) = \mathrm{sgn}_+(\cos(\varphi - a))$ and $B(b, \varphi) = \xi\,\mathrm{sgn}_+(\cos(\varphi - b))$ disagree on total phase measure 2η, so

$$P_{\mathrm{diff}}(\eta) = \frac{\eta}{\pi}, \qquad E^{(\xi)}_{\mathrm{tri}}(\eta) = \xi\left(1 - \frac{2\eta}{\pi}\right), \tag{19}$$

exactly, for the stated uniform phase and sign readout. For ideal linear-polarisation quantum measurements with the same convention the kernel is $E^{(\xi)}_{\mathrm{QM}}(\eta) = \xi\cos\eta$.

5.2 The exact core: one state, one projection, two readouts

At $\theta_v = 0$ the analog signals are $g_A = \cos(\varphi - a)$ and $g_B = \xi\cos(\varphi - b)$; their covariance over the phase circle is $\frac{\xi}{2}\cos\eta$ and each standard deviation is $1/\sqrt{2}$, so

$$\boxed{C_P(\eta) = \xi\cos\eta} \tag{20}$$

exactly, for every η. The analog ledger of the local helix is the quantum kernel, not an approximation to it. Substituting $\eta = \arccos C_P$ into Eq. (19),

$$\boxed{E_{\mathrm{bin}} = \frac{2}{\pi}\arcsin C_P} \tag{21}$$

the Van Vleck / Grothendieck arcsine law: the sign function is the lossy step, and the loss is the universal cost of binarising a planar projection. For the triangle kernel at settings separated by $(\eta, \eta, \eta, 3\eta)$,

$$S_{\mathrm{tri}}(\eta) = 3\left(1 - \frac{2\eta}{\pi}\right) - \left(1 - \frac{6\eta}{\pi}\right) = 2 \qquad \text{identically on } 0 \le \eta \le \pi/3, \tag{22}$$

so the model rides the local bound along a continuum rather than touching it at a point (beyond $\pi/3$ the fourth separation folds and S_{tri} falls below two). Taking each kernel's CHSH at its own optimum,

$$\max_\eta S_{\mathrm{tri}} = 2, \qquad \max_\eta S_{\cos} = 3\cos\tfrac{\pi}{4} - \cos\tfrac{3\pi}{4} = 2\sqrt{2}, \qquad \frac{\max S_{\cos}}{\max S_{\mathrm{tri}}} = \sqrt{2} = K_G(2), \tag{23}$$

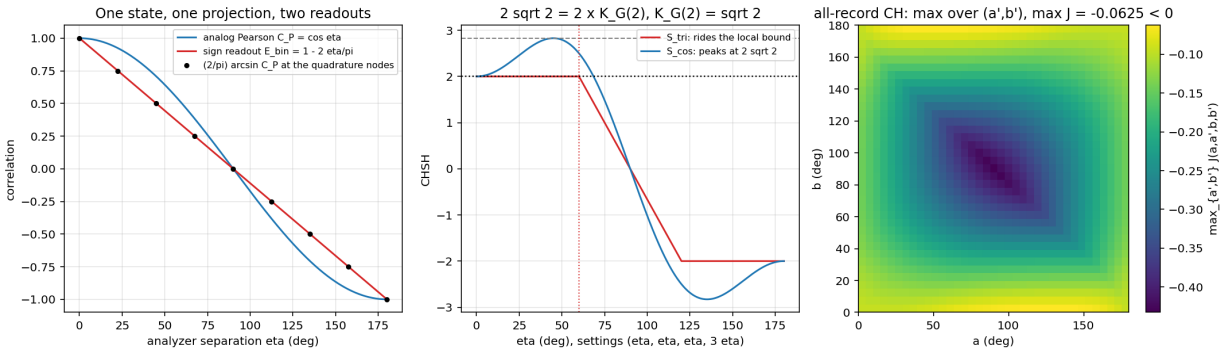


Figure 2: The exact core. Left: at top view the same source supports two readouts — the analog Pearson correlation is exactly $\cos\eta$, the sign record is exactly the triangle, and the arcsine law relates them. Centre: S_{tri} rides the local bound identically on $\eta \le \pi/3$ while $S_{\cos}$ peaks at $2\sqrt{2}$; the ratio is $K_G(2) = \sqrt{2}$. Right: the all-record Clauser–Horne landscape at the aperture ridge, $\max_{a',b'} J(a,a',b,b')$ over (a,b), everywhere negative.

Krivine's exact Grothendieck constant of order two [9]: the supremum of the ratio between the vector-valued and the ± 1 CHSH value for correlations built from planar unit vectors. Tsirelson's bound is the local bound times the rounding constant of the plane, $2\sqrt{2} = 2 \times \sqrt{2}$ [8]. The exact-core exhibit evaluates Eqs. (20)–(23) by midpoint quadrature with 4×10^6 phase nodes: residuals 1.1×10^{-16} for $C_P - \cos\eta$, 0 for the triangle, 1.1×10^{-16} for the arcsine law, 4.4×10^{-16} for the plateau, and $\max S_{\cos} = 2.828427125$, ratio 1.414213562 (Fig. 2, left and centre).

5.3 Counterfactual per-state identity

For jointly assigned potential outcomes $A, A', B, B' \in \{-1, +1\}$, $C = AB - AB' + A'B + A'B' = A(B - B') + A'(B + B') \in \{-2, +2\}$: generic binary CHSH algebra. The common-counterfactual simulator evaluates all four terms on one hidden state and obtains a zero-variance mean for this quantity; a laboratory randomised-setting experiment observes one setting pair per event and has a different estimator and uncertainty.

5.4 One-floor oblique-view law

With the normalised view coordinate $q = \theta_v/(\pi/2) \in [0, 1]$ and $u(\varphi) = \varphi/2\pi - 1/2$, a pair separated by one floor has

$$s_A(\varphi; q) = \cos\tfrac{\pi q}{2} \cos\varphi + p_r \sin\tfrac{\pi q}{2}\, u(\varphi), \qquad s_B = s_A + p_r \sin\tfrac{\pi q}{2}, \tag{24}$$

RMS signal difference $D_{\mathrm{RMS}}(q) = p_r \sin(\pi q/2)$, equal to $p_r/\sqrt{2}$ at $q = 1/2$, and binary correlation

$$E_{p_r}(q) = 1 - \frac{1}{\pi} \int_0^{2\pi} \mathbf{1}\{-p_r \sin\tfrac{\pi q}{2} < s_A(\varphi; q) < 0\}\, d\varphi. \tag{25}$$

Midpoint quadrature with $M = 2{,}000{,}000$ nodes followed by bisection in q gives the roots in Table 3; the archive values are the first threshold hits on a 121-point grid with $\Delta q = 1/120$.

p_r	midpoint root q^*	first archive grid hit	$D_{\mathrm{RMS}}(1/2)$
0.10	0.90982	0.91667	0.07071
0.25	0.78197	0.78333	0.17678
0.50	0.60565	0.60833	0.35355
1.00	0.38931	0.39167	0.70711
2.00	0.21467	0.21667	1.41421

Table 3: One-floor $E = 0.5$ crossing in the normalised view coordinate.

6 Numerical geometry and detection studies

6.1 View sweep with a fixed source state

The v16 sweep changes only the local projection angle. For the $\xi = +1$ orientation the top-view simulated kernel agrees with Eq. (19) to RMS 0.001121. On the released 49-point view grid the all-record CHSH magnitude is bounded by two, with maximum 2.000000 — the plateau of Eq. (22) — and minimum 1.605584; the bound is view-independent, the curve is not view-flat (Fig. 3).

6.2 The Q fiducial and the common-rotation control

Equation (11) ties the axial coordinate to the azimuth measured from the origin φ_0, so at oblique view the source has an absolute azimuth: a common rotation of both analyzers at fixed separation changes the binary correlation. With $\varphi_0 = 0$, matched 30° views, 45° separation, zero energy and 280,000 shared-start events, $E = 0.498364, 0.451521, 0.453450, 0.495414, 0.500143$ at common rotations $0°, 45°, 90°, 135°, 180°$, a spread of 0.0486 (20 paired standard errors), while the largest single-wing mean is 0.0287; top view is invariant. This is the predicted anisotropy of the Q fiducial: a device that supplies an axial floor coordinate (Protocol P3) reads the start azimuth of the helix. With `-random-azimuth` the origin is drawn per pair and the spread falls to 1.7 paired standard errors: the randomised-origin ensemble is rotation-invariant and is the control against which the anisotropy is measured.

6.3 Local interface rules

The simulation family contains two local interface models. A single-channel Malus model uses unit Poincaré/Bloch vectors $\widehat{\mathbf{a}}, \mathbf{s} \in S^2$ and the local probability $p_M = (1 + \widehat{\mathbf{a}} \cdot \mathbf{s})/2$; for equatorial linear polarisations $p_M = \cos^2 \Delta\theta_{\mathrm{lab}}$. A transported deterministic coordinate and a fresh local random variable both reproduce that singles curve; the curve alone does not identify the event mechanism.

For the aperture calculation let $u_{\mathrm{sph}}, z_A, z_B \sim \mathrm{Unif}(0,1)$ independently and $\phi_{\mathrm{sph}} \sim \mathrm{Unif}[0, 2\pi)$. With $\kappa = k_{\mathrm{bias}} > 0$,

$$s_z = \sin\left(\frac{\arcsin(2u_{\mathrm{sph}} - 1)}{\kappa}\right), \qquad \mathbf{s} = \left(\sqrt{1 - s_z^2}\cos\phi_{\mathrm{sph}}, \sqrt{1 - s_z^2}\sin\phi_{\mathrm{sph}}, s_z\right). \tag{26}$$

The ridge calculation uses the anticorrelated pair $\mathbf{s}_A = \mathbf{s}$, $\mathbf{s}_B = -\mathbf{s}$ with unit analyzer vectors $\widehat{\mathbf{a}}, \widehat{\mathbf{b}}$. The clipped local aperture law is

$$p_{\mathrm{acc}}(\widehat{\mathbf{a}}, \mathbf{s}_A) = \mathrm{clip}_{[0,1]}(\rho_s + (\rho_r - \rho_s)|\widehat{\mathbf{a}} \cdot \mathbf{s}_A|), \tag{27}$$

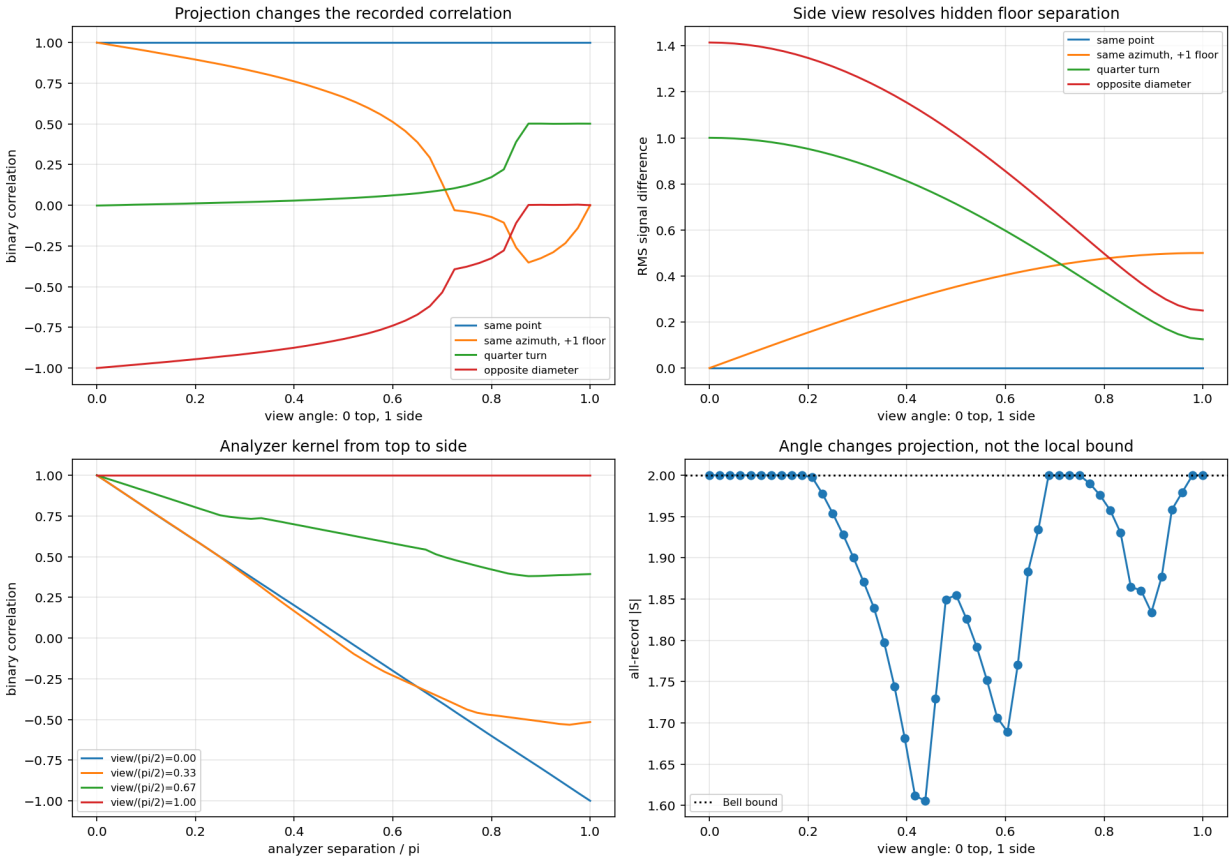


Figure 3: v16 projection sweep. Binary pair correlations, RMS signal differences, analyzer-kernel deformation, and the all-record common-counterfactual CHSH statistic as the view angle changes with the source geometry fixed. The CHSH curve stays at or below two and varies with view angle; only its upper bound is view-independent.

with records $A = \mathrm{sgn}_+(\hat{\mathbf{a}} \cdot \mathbf{s}_A)$, $D_A = \mathbf{1}\{z_A < p_{\mathrm{acc}}\}$ and the analogous expressions at Bob's wing. All source and gate variables belong to the hidden state λ of the common-ensemble proof. ρ_s and ρ_r are the raw aperture intercept and the endpoint at unit alignment; $k_{\mathrm{bias}} = 1$ is the uniform sphere and larger values compress the source toward the equator. Neither coefficient is an α and neither lies in $[0, 1]$ by requirement; the gate probability is p_{acc} after clipping. The gate depends on $\hat{\mathbf{a}}$: whether an event is counted depends on which question was asked, which is the mechanism of the accepted-pair excess. At $(\rho_s, \rho_r, k_{\mathrm{bias}}) = (0.2750, 1.4375, 1.5)$ about 49.1% of the tested local threshold values reach the upper clipping boundary. Figure 4 displays the transport, projection and ledger results.

6.4 Finite aperture ridge

With $\varepsilon_{\mathrm{wing}}$ the mean of the four marginal gate frequencies and $\varepsilon_{\mathrm{joint}}$ the mean of the four coincidence frequencies, the archive's 20-seed summary at 3×10^6 states per seed reports seed standard deviations $\varepsilon_{\mathrm{wing}} = 0.82803 \pm 0.00010$, $|S|_{\mathrm{acc}} = 2.82842 \pm 0.00054$. The complete eight-seed ledger (seeds $3000, \ldots, 3007$, 2×10^6 states each, same event indices for the four setting pairs, gate arrays reused

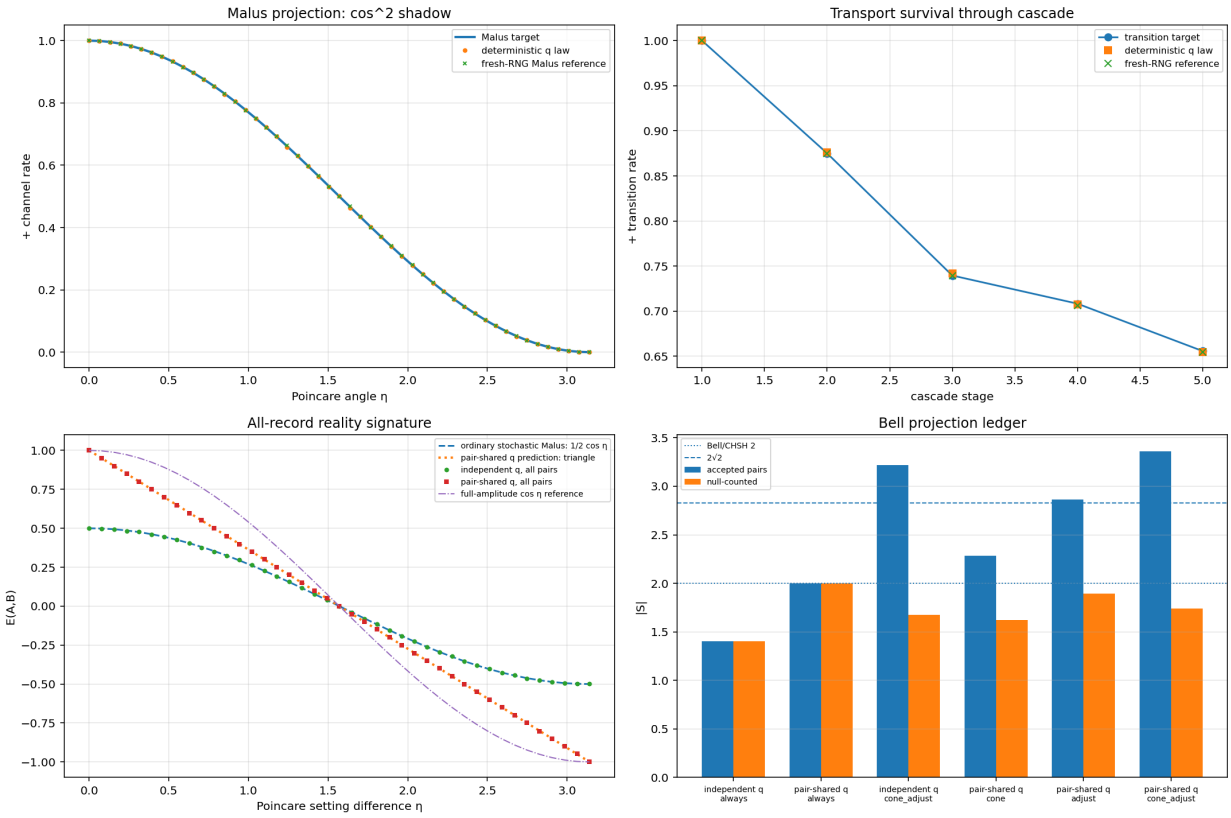


Figure 4: Transport, projection, and Bell-ledger results from the statistical closure simulation. The lower-left panel separates the pair-shared triangular all-record kernel from the half-amplitude and full-amplitude cosine references; the lower-right panel places accepted-pair and null-counted CHSH values side by side — values above two occur only in the coincidence-conditioned bars.

only within their own wings) is

$$\begin{aligned} |S|_{\mathrm{acc}} &= 2.828275 \pm 0.000343, & |S|_0 &= 1.911389 \pm 0.000153, \\ \varepsilon_{\mathrm{wing}} &= 0.828058 \pm 0.000068, & \varepsilon_{\mathrm{joint}} &= 0.675814 \pm 0.000103, \end{aligned} \tag{28}$$

every uncertainty a seed SD. The exact-core exhibit reimplements this calculation blind from the specification of Appendix A and reproduces every published digit, with $\varepsilon_{\mathrm{joint}}|S|_{\mathrm{acc}} - |S|_0$ averaging 3×10^{-7}: the ledger separates the accepted-pair match to $2\sqrt{2}$ from the all-trial statistic by exactly the selection factor. The symmetric maximally-entangled critical efficiency $\eta_{\mathrm{GM}} = 2(\sqrt{2}-1) = 0.828427$ [11, 14] sits 5.5 seed SDs above $\varepsilon_{\mathrm{wing}}$: a near miss, not a coincidence to be claimed. The ridge is a finite selected-aperture calculation; another archived point $(0.25, 1.5, 1.5)$ has $\varepsilon_{\mathrm{wing}} = 0.82970$ and $|S|_{\mathrm{acc}} = 2.8388$, permitted because the statistic is coincidence-conditioned, and neither a Tsirelson violation nor an all-record one [8].

7 Scheduled and separated-time source studies

The rotating-gate program schedules the start phase and, in its fully deterministic mode, the local coordinates with shifted windows of Weyl sequences. Across eight replicate windows at $N = 5.12 \times 10^6$ the stored sample SD is 5.76×10^{-4} for random sampling and 3.1×10^{-5} for the fully scheduled

calculation: numerical integration of a discontinuous accepted-pair estimator. The shifted windows are not independent physical trials and the ratio is not a laboratory noise floor. For Gaussian jitter of the pair's relative orientation the unconditioned cosine target is $S_{\mathrm{nom}}(\sigma_\varphi) = 2\sqrt{2}e^{-\sigma_\varphi^2/2}$; the postselected aperture simulation returns 2.7162 and 2.5272 at $\sigma_\varphi = 0.30, 0.50$ against 2.7040 and 2.4961, so the exponential is a comparison curve, not an exact law of the selected simulation.

The separated-time program imposes matched, antimatched, or independent hidden-state schedules on two simulated emissions. Over ten seeds with 2,000,000 states per seed the accepted-pair CHSH magnitude is 2.82839 ± 0.00040 for the matched schedule and 0.00098 ± 0.00073 for the independent schedule; the partial-match sweep is linear in the match fraction. These are conditional correlations generated with an explicit shared schedule — a classical common cause in the simulation — and separation in time alone does not require a conventional comparison state to have zero correlation. An experimental FDT-entanglement claim requires an operational reconstruction of the shared-origin or matched-gradient condition of Eq. (8) with declared transport, matching, tolerance and uncertainty (Protocol P5); a Bell-nonlocality claim additionally requires an event-ready or all-record inequality, independent random settings, per-setting efficiencies and remote-setting marginals.

8 Transport of the shared bivector grade

8.1 The derived generator

Under the aperture assignment $n = n_{\mathrm{cone}}(\alpha_n)$ in a smooth isotropic medium, Fermat's principle gives $d(n\mathbf{t})/ds = \nabla n$ for the unit ray tangent $\mathbf{t}$, and the minimal (twist-free) frame along the ray rotates with

$$\boldsymbol{\Omega} = \mathbf{t} \times \nabla \ln n = \frac{\mathbf{t} \times \nabla \alpha_n}{2(1-\alpha_n)}, \qquad B = \mathbf{t} \wedge \nabla \ln n = \frac{\mathbf{t} \wedge \nabla \alpha_n}{2(1-\alpha_n)}, \qquad \frac{dR}{ds} = -\frac{1}{2} B R, \tag{29}$$

later increments multiplying on the left, $R_{\mathrm{total}} = R_{\mathrm{last}} \cdots R_{\mathrm{first}}$ [31, 30]. The event plane is $\mathbf{t} \wedge \nabla \alpha_n$ — the bivector grade of the density gradient along the ray — and the rotation per unit length is $|\boldsymbol{\Omega}|$. The ray equation leaves an axial twist $\chi \mathbf{t}$ undetermined; the packages take $\chi = 0$. The solver reproduces the exact stratified-exponential-index solution (bend, conserved transverse optical momentum, optical path) to 6×10^{-16}. Two consequences carry the rest of the paper.

Density alone rotates nothing. $n \to c\,n$ leaves $\nabla \ln n$, the rays, the rotors and the endpoint maps unchanged while the optical path scales by c: in the v19 run the state trace distance and the maximum Jones-map difference under $n \to 2n$ are exactly zero at every point of the α_n sweep. The gradient in Eq. (8) is the right object.

Order matters. The second Magnus term $\frac{1}{8}\iint_{s_2<s_1}[B(s_1), B(s_2)]$ vanishes for one fixed plane and not otherwise; equal scalar α_n histograms, equal RMS fluctuation and equal $\int n\,ds$ do not fix the rotor product. Physically reordering two gradient regions recomputes the trajectory and the gradients it samples, and changes the final frame by 0.030909 rad in the archived example. Profile nonuniqueness is exact both ways: distinct monotone $\alpha_n(s)$ with equal endpoints and equal $\int n\,ds$ give identical phase, refraction and records in a scalar detector. The predicate is therefore ordered and pointwise by necessity.

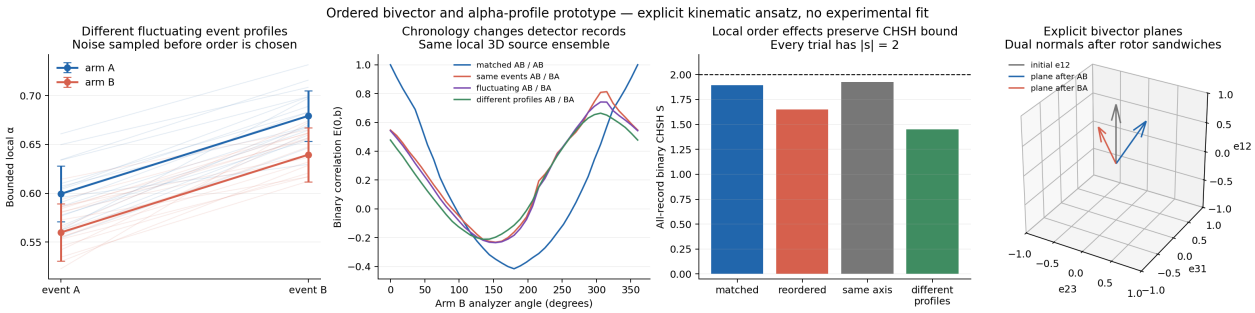


Figure 5: Ordered-bivector prototype. Different fluctuating event profiles in the two arms; chronology changes the detector records on the same local source ensemble; local order effects preserve the CHSH bound with every trial at $|s| = 2$; the explicit bivector planes after the two orders.

8.2 The conservation theorem

Theorem 1 (Conservation of the shared bivector grade)**.** *Let two identical carriers leave a shared origin with matched transverse frames and traverse paths γ_A, γ_B in media whose transported gradients coincide pointwise and in order, $\Pi_\tau \nabla\alpha_n|_{\gamma_B(f(\tau))} = \nabla\alpha_n|_{\gamma_A(\tau)}$. Then $R_A(\tau) = R_B(\tau)$ for all τ, the endpoint maps coincide, $J_A = J_B$, and the joint polarisation state is the emitted state exactly: the singlet is invariant under $U \otimes U$ for every $U \in SU(2)$. Conversely, for unresolved real $SO(2)$ endpoint rotations β_A, β_B the ensemble state has*

$$\mathcal{N} = \frac{|\gamma|}{2}, \qquad \mathrm{Tr}\,\rho^2 = \frac{1+|\gamma|^2}{2}, \qquad \gamma = \langle e^{2i(\beta_A - \beta_B)} \rangle,$$
$$S_{\max,\mathrm{qubit}} = 2\sqrt{1+|\gamma|^2}, \qquad S_{\max,\mathrm{linear}} = 2\sqrt{2}|\gamma|, \qquad S_{\mathrm{fixed}} = 2\sqrt{2}\,\mathrm{Re}\,\gamma. \tag{30}$$

The first part is Eq. (29) with the singlet's $U \otimes U$ invariance; the second is direct diagonalisation for the real-Jones subclass (negativity in the sense of [29]; the qubit maximum by the Horodecki criterion). The v19 run verifies Eq. (30) to 5×10^{-15} at every scenario and sweep point, and every scenario with matched histories returns negativity 0.5 and $S = 2\sqrt{2}$ at the optimal linear analyzers with bitwise-equal Jones maps. Theorem 1 is the entanglement predicate of Eq. (8) written as a conservation law, and it is I-4's "shared bivector grade" written as an equation.

8.3 The ordered-bivector prototype

Carrying the oriented plane and the detector probe through the same chronological rotor product (30,000 events; the exploratory event-angle coupling $\theta = \mathrm{gain} \cdot \mathrm{duration} \cdot [n_{\mathrm{cone}}(\alpha_n) - n_{\mathrm{ref}}]$ retained as a separately testable predictor beside the derived generator): identical histories give plane alignment 1.00000 and $E(0,0) = 1.00000$; the same deterministic events in reversed order in one arm give alignment 0.74473, $E(0,0) = 0.54693$, a relative-rotor angle of 0.74509 rad and a change in 22.65% of equal-setting records; the same-plane commuting control gives 1.00000; remote order changes leave the untouched arm array-identical; every trial keeps $|s| = 2$ (Fig. 5). The rotor implementation agrees with an independent rotation library to 1.8×10^{-15}.

Field history comparison	negativity	fixed-analyzer S	cylinder S
Uniform fluctuating density (no gradient)	0.500000	2.828427	2.000000
Identical spatial fields and bases	0.500000	2.828427	2.000000
Independent fields, nominal $\alpha_n = 0.4/0.4$	0.309728	1.750213	1.364052
Coefficient correlation 0.5, same marginals	0.332705	1.882047	1.447986
Shared coefficients, nominal $\alpha_n = 0.2/0.8$	0.256879	1.450123	1.127653
Independent fields, nominal $\alpha_n = 0.2/0.2$	0.453294	2.563461	1.887369
Independent fields, nominal $\alpha_n = 0.8/0.8$	0.115175	0.651283	0.529043
Matched gradient-region order, logit noise 0.25	0.500000	2.828427	2.000000
One arm's regions reordered, logit noise 0.25	0.488372	2.759170	1.961892

Table 4: v19 ensemble results. "Cylinder S" is the separate local half-circle threshold readout on the transported plane with a uniform, clamp-independent phase, whose per-trial support is $\{-2, +2\}$ in every scenario; on the projection measure of the host clamp the same readout returns the fixed-analyzer column (Sec. 10). The conservative pointwise 95% Monte Carlo interval for the independent-field negativity is $[0.2563, 0.3631]$.

9 Fluctuating media: conservation, ignorance, fragility

9.1 The field-to-detector chain

The v19 stage draws differentiable three-dimensional fields $q(\mathbf{r}) = \operatorname{logit} \alpha_n(\mathbf{r})$ from a finite Gaussian Fourier law (18 modes at 0.18 m; logit noise 0.8; paired coefficients with a declared cross-arm correlation), so that $\nabla \alpha_n = \alpha_n(1 - \alpha_n)\nabla q$ and $\nabla \ln n = \frac{1}{2}\alpha_n \nabla q$ are analytic — the load map written pointwise on the odds. Each ray is traced through its own realised field over 1 m at 2 mm steps under Eq. (29); a declared Jones map $J = V_{\text{out}}^{\mathsf{T}} Q V_{\text{in}}$ carries the frame into the Born layer — the phase-ignorance projection statistics of the helix, which the settlement of Sec. 10 returns cell by cell — and a three-outcome detector layer (+, −, no click) keeps all nine outcome pairs per setting pair with declared port efficiencies, label confusion and pair-emission probability. Table 4 gives the ensemble results over 1,536 paired histories per scenario (Fig. 6).

9.2 Decoherence is ignorance of the relative history

Every resolved history preserves the pair exactly (negativity 0.5 in every scenario and sweep point). The reductions in Table 4 appear only when the history is discarded and density matrices are averaged, by Eq. (30); applying the measured inverse local maps before averaging restores the singlet. Nothing physical is lost; the record is. This is I-4's reading of superposition as phase ignorance extended to the pair, and it is deterministic and local. A whole-photon scalar phase cancels from the polarisation density matrix; the channel is the relative bivector history. Shared coefficients on unequal baselines (0.2/0.8) lose negativity to 0.257 although the drive is common, because the responses $\nabla \ln n = \frac{1}{2}\alpha_n \nabla q$ differ; identical local Jones maps protect the singlet exactly at any noise amplitude.

9.3 The density-fragility law

With the fluctuation amplitude fixed in the logit (odds) coordinate, the geometric drive grows with the baseline, $|\nabla \ln n| = \frac{1}{2}\alpha_n |\nabla q|$, and the ensemble negativity under independent fluctuations falls monotonically with it (Table 5). At every point $n \to 2n$ at fixed $\nabla \ln n$ leaves the negativity

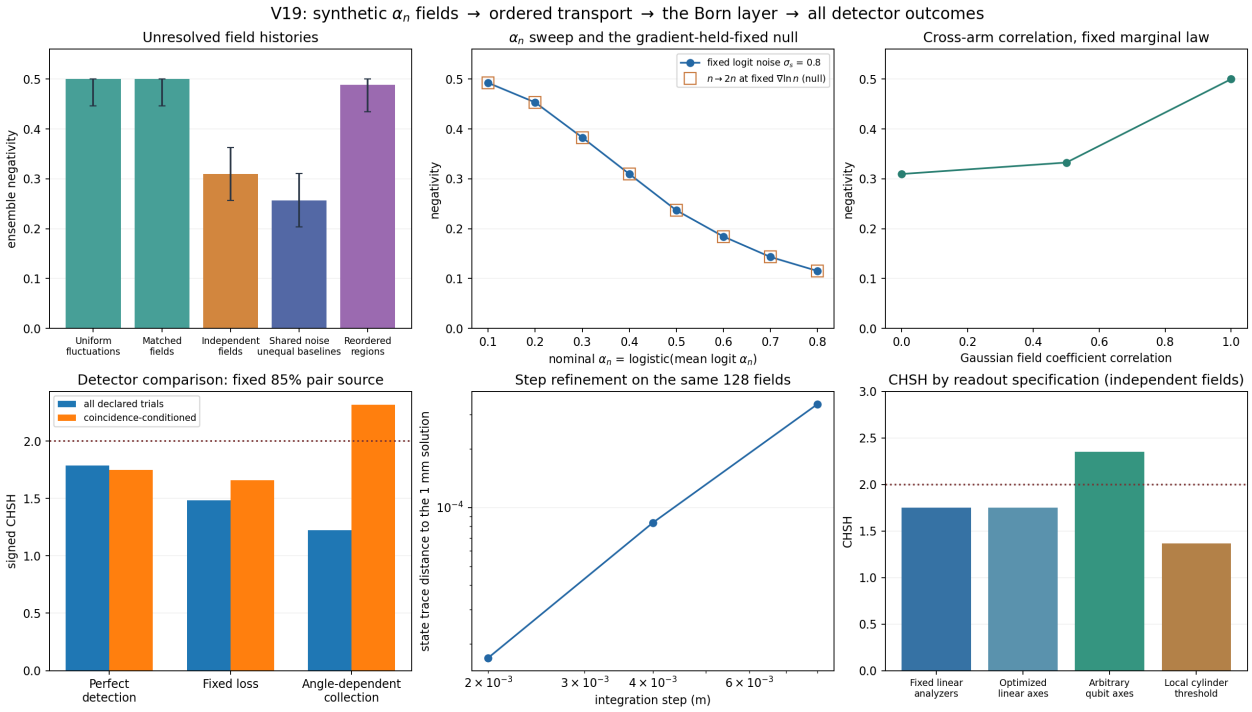


Figure 6: v19 gradient transport. Ensemble negativity by scenario with conservative Hoeffding whiskers; negativity against nominal α_n with the $n \to 2n$ gradient-held-fixed null on the same realisations; negativity against the cross-arm coefficient correlation; all-trial versus coincidence-conditioned CHSH by detector model; step refinement; CHSH by readout specification.

nominal α_n	0.1	0.2	0.3	0.4	0.5	0.6	0.7	0.8
RMS drive $\lvert\nabla \ln n\rvert$ in arm A (m^{-1})	0.559	1.037	1.466	1.852	2.207	2.544	2.871	3.184
negativity, independent fluctuations	0.4925	0.4533	0.3829	0.3097	0.2368	0.1843	0.1432	0.1152
negativity after $n \to 2n$ at fixed $\nabla \ln n$	0.4925	0.4533	0.3829	0.3097	0.2368	0.1843	0.1432	0.1152
fixed-analyzer S	2.786	2.563	2.166	1.750	1.336	1.039	0.807	0.651

Table 5: The α_n sweep of v19 (logit noise 0.8, 1,536 paired histories per point). The gradient-held-fixed null leaves every row of the third line unchanged.

unchanged: the fragility is carried by the gradient drive, and the α_n prefactor is what a denser baseline adds.

Entanglement is more fragile in a denser medium. Any hand that raises the medium's index raises α_n, shortens entanglement survival under independent fluctuations and breaks the common-mode protection between unequal arms. The sign is on the index: the arm whose medium carries the higher index loses agreement faster at fixed common drive. Compression raises the index of every ordinary medium and is the clean hand; an isotope or a thermal change acts through the medium's own optical response, whose sign is the medium's — the I-7 discipline, the input signed and the displayed sign following the sensitivities (Protocol P6).

9.4 Selection inside the Born layer

With the fixed 85% pair source and the independent-field state, the all-trial / coincidence-conditioned CHSH pairs are 1.787681/1.750213 (perfect detection), 1.482804/1.660082 (fixed port

losses and label confusion) and 1.223112/2.316859 (collection depending on the local ray angle): the selection mechanism of Sec. 4.2 reappears inside the Born layer, and a coincidence value is not interchangeable with the all-trial Bell statistic. Averaging state and acceptance separately instead of per history changes one joint cell by 0.00911 and gives 1.085806 instead of 1.223112; the packages keep the paired history.

10 The projection settlement

10.1 The measure

The cylinder readout of Sec. 9 keeps two records on one shared phase on the doubled-angle circle of the helix chart,

$$A = \operatorname{sgn}_+ \cos(\varphi + 2\beta_A - a), \qquad B = \operatorname{sgn}_+ \cos(\varphi + \pi + 2\beta_B - b), \tag{31}$$

the partner carried at $\varphi + \pi$: the shared bivector grade, opposite sense. With φ uniform and independent of the clamps these records return the triangle of Eq. (19) and $S = 2$. The records are kept as they stand. The core supplies the measure of the shared phase (I-4, v6.7 [2]). I-4 reads the wavefunction as the projection of the helix onto the plane normal to the axis, and a clamp — an analyzer, a boundary condition of P-2 — reads the helix in that projection: the clamp at a is the cut $\cos(\varphi - a) = 0$, and the coordinate across the cut is the projected one, $x = \sin(\varphi - a) \in [-1, 1]$. The pair and its two clamps are one system, and the pair's record is one settlement of it (0.1a), its mode geometry set by the clamps (P-2). For the equal-weight pair the settlement lands uniformly across the projected aperture of the clamp that hosts it, x uniform on each of the two sheets:

$$\boxed{p_{\text{host}}(\varphi \mid a) = \frac{|\cos(\varphi - a)|}{4}} \qquad p(\varphi_A, \varphi_B \mid a, b) = \delta(\varphi_B - \varphi_A - \pi)\, p_{\text{host}}(\varphi_A \mid \text{host clamp}). \tag{32}$$

With transport the measure is $|\cos u|/4$ in the host's impact phase, $u_A = \varphi + 2\beta_A - a$ or $u_B = \varphi + \pi + 2\beta_B - b$, and the shared phase is its pull-back through that arm's Jones rotation. Ignorance of the phase is ignorance of where across the aperture the settlement lands. Uniform in the projected coordinate is the projection measure; uniform in the angle, $1/2\pi$, is the clamp-independent reading; the two differ by the change of variable $\varphi - a = \arcsin x$.

10.2 The kernel

Theorem 2 (Cosine kernel of the settlement)**.** *Let* $\Delta = a - b - 2(\beta_A - \beta_B)$*. On the measure of Eq.* (32) *the records of Eq.* (31) *satisfy*

$$P(A = B) = \frac{1 - \cos\Delta}{2}, \qquad E_{\text{set}}(\Delta) = -\cos\Delta, \qquad P(A = +1) = P(B = +1) = \frac{1}{2}, \tag{33}$$

for either host clamp and for every mixture of hosts.

Proof. Take host A. In its impact phase $A = \operatorname{sgn}_+ \cos u$ and $B = -\operatorname{sgn}_+ \cos(u + \Delta)$. For $0 \le \Delta \le \pi$ the two records are equal on the arc $\pi/2 - \Delta < u < \pi/2$ and on its antipode, each of mass $\int_{\pi/2-\Delta}^{\pi/2} \frac{1}{4} \cos u \, du = (1 - \cos\Delta)/4$; evenness and periodicity in Δ cover the rest. The measure is invariant under $u \mapsto u + \pi$, which reverses both records, so each record is ± 1 with probability $1/2$

Measure of the shared phase	$S\pm$ counting SE	exact S	records kept
Projection, host A	2.828730 ± 0.001414	2.828427	4,000,000/4,000,000
Projection, host B	2.829470 ± 0.001414	2.828427	4,000,000/4,000,000
Projection, either host	2.827638 ± 0.001414	2.828427	4,000,000/4,000,000
Uniform, clamp-independent	2.000188 ± 0.001732	2.000000	4,000,000/4,000,000

Table 6: All-record CHSH of the cylinder sign records at $a = (0, \pi/2)$, $b = (-3\pi/4, 3\pi/4)$. Sampled single-wing frequencies sit within 0.0012 of 1/2 in every row.

at every clamp pair. Host B is the same computation in u_B with $\Delta \mapsto -\Delta$, and a mixture of hosts is a mixture of two equal tables. □

The same computation with the uniform measure gives $P(A = B) = |\Delta|/\pi$, the triangle. The two kernels are the two sides of the arcsine law, Eq. (21): the uniform angle returns $-(2/\pi) \arcsin \cos \Delta$, the projection measure returns $-\cos \Delta$. Each wing's record reads its own clamp and the phase it receives, and no single-wing record carries a reading of the remote clamp. No order of the two records enters the statistics.

The v20 stage evaluates Eq. (33) by exact arc integration — the antiderivative of the measure between the sign boundaries, with no closed form of the kernel in the code — on 1,441 points of $\Delta \in [-2\pi, 2\pi]$: the largest $|E_{\text{set}} + \cos \Delta|$ is 5.6×10^{-16}, the marginals sit at 1/2 to 1.1×10^{-16}, and the tables for host A, host B and host mixtures of weight $0, \frac{1}{4}, \frac{1}{2}, \frac{3}{4}, 1$ agree to 1.7×10^{-16}. At the clamps $a = (0, \pi/2)$, $b = (-3\pi/4, 3\pi/4)$ the settlement gives $S = 2.828427125$ and the uniform measure $S = 2.000000000$; their ratio is $1.414213562 = K_G(2)$. Over 331,776 clamp quadruples on a 15° grid and the four CHSH facets the largest $|S|$ is 2.828427125 for the settlement and 2.000000000 for the uniform measure.

10.3 Every record kept

Table 6 is the event-by-event ledger at those clamps: one million records per setting pair, four setting pairs, and all 4,000,000 records of each row in the statistic.

Reading all four clamp positions on one phase gives $A_0B_0 + A_0B_1 + A_1B_0 - A_1B_1 = \pm 2$ at every sampled phase of every row, the settlement rows included: the arithmetic of Eq. (15) holds phase by phase. The uniform row averages that quantity over one measure and stays at 2. The settlement's four correlators are averages over the measures of the two host settings, and the bound of Sec. 4, whose premise is $\rho(\lambda \mid a, b) = \rho(\lambda)$, does not constrain them.

10.4 The price of the clamp route

The measure is set by a clamp. In Hall's measure of measurement dependence [18], $M = \sup \int |\rho_{xy} - \rho_{x'y'}| \, d\lambda$, with M_1 varying A's clamp at fixed B's and M_2 the reverse, a settlement hosted at A has $M_2 = 0$ and

$$M_1 = \sup_{a,a'} \int_0^{2\pi} \left| p_{\text{host}}(\varphi \mid a) - p_{\text{host}}(\varphi \mid a') \right| d\varphi = \int_0^{2\pi} \frac{\big| |\cos\varphi| - |\sin\varphi| \big|}{4} \, d\varphi = 2\sqrt{2} - 2 = 0.828427, \tag{34}$$

the supremum at clamps a quarter turn apart, with $F = 1 - M_1/2 = 2 - \sqrt{2} = 0.585786$.

Proposition 1 (One-sided bound)**.** *For a measure ρ_x set by A's clamp alone and any records $A_x, B_y \in \{-1, +1\}$ on it,*

$$S = \int \rho_0 A_0 (B_0 + B_1) + \int \rho_1 A_1 (B_0 - B_1) \;\le\; 2 + \int (\rho_0 - \rho_1) B_0 B_1 \;\le\; 2 + M_1. \tag{35}$$

Proof. $|B_0 + B_1| = 1 + B_0 B_1$ and $|B_0 - B_1| = 1 - B_0 B_1$, so $S \le \int \rho_0 (1 + B_0 B_1) + \int \rho_1 (1 - B_0 B_1)$; the second step is $|B_0 B_1| = 1$. □

This is the one-sided relaxed Bell inequality [20]. The settlement meets both steps with equality at the Tsirelson clamps: $B_0 B_1 = \operatorname{sgn}(\rho_0 - \rho_1)$ on the whole circle, $\int (\rho_0 - \rho_1) B_0 B_1 \, d\varphi = 0.828427125 = M_1$, and $S = 2 + M_1 = 2\sqrt{2}$ (slack 1.2×10^{-12} by midpoint quadrature). The equality is not special to the quarter turn. For host clamps an angle θ apart, $0 \le \theta \le \pi$, the integral of Eq. (34) is

$$M_1(\theta) = 2\big(\sin\tfrac{\theta}{2} + \cos\tfrac{\theta}{2}\big) - 2 = 2\sqrt{1 + \sin\theta} - 2, \tag{36}$$

and with A's clamps at that separation the largest S over B's clamps on the kernel $-\cos\Delta$ is $2\cos\frac{\theta}{2} + 2\sin\frac{\theta}{2} = 2\sqrt{1 + \sin\theta} = 2 + M_1(\theta)$: the bound of Proposition 1 is met at every pair of host clamps, and the excess of the settlement over the local bound is the distance between the two measures, never more and never less. Since $M_1 \le 2\sqrt{2} - 2$ for every pair of host clamps,

$$S \;\le\; 2 + M_1 \;\le\; 2\sqrt{2} \qquad \text{on every clamp quartet:} \tag{37}$$

Tsirelson's value is the ceiling of the projection measure, and the excess of that ceiling over the local bound is the distance between the measures of two clamps a quarter turn apart. A measure free to depend on both clamps obeys $S \le 2 + 3M$ and reaches 4 at $M = 2/3$ [18], so $2\sqrt{2}$ there needs $M \ge (2\sqrt{2} - 2)/3 = 0.276142$; the projection measure stops at $2\sqrt{2}$. $F = 2 - \sqrt{2} = 58.6\%$ is the optimum for a measure set by one side that returns the singlet table [19]; a measure set by both sides returns it at $F = 86\%$ [18]. The mutual information between the phase and the host clamp is 0.201752 bits for two equiprobable clamps and 0.208801 bits for a clamp uniform on the circle. $M_1 = 2(\sqrt{2} - 1)$ is also the Garg–Mermin efficiency of Sec. 4.2 [11]: with $\eta_{\mathrm{GM}} = 4/(S + 2)$ and $M_1 = S - 2$ the two coincide where $(S - 2)(S + 2) = 4$, at $S = 2\sqrt{2}$ and at no other value. One number prices fair sampling and the other measurement independence. The prediction of the route: on every all-record ledger of the equal-weight pair the kernel is $-\cos\Delta$ at unit visibility and $|S| \le 2\sqrt{2}$; an all-record CHSH above $2\sqrt{2}$, or a unit-visibility kernel other than $-\cos\Delta$, falsifies the measure.

10.5 The same weight by selection

The weight $|\cos(\varphi - a)|$ applied as a local acceptance on a uniform phase is a detection-selected model [24]. With one million records per setting it gives accepted-pair $S = 2.828682$ at wing efficiency 0.636600 ($2/\pi = 0.636620$) and $S = 1.800740$ with nulls scored 0: the selection identity of Lemma 1 at $\varepsilon = 2/\pi$. The aperture law of Eq. (27) is the clipped affine form of the same weight on the sphere, $\rho_s + (\rho_r - \rho_s)|\widehat{\mathbf{a}} \cdot \mathbf{s}_A|$. Selection reaches the measure by dropping records and stays under 2 on all records. The settlement carries the same measure on every record.

10.6 Transport, detectors and arbitrary axes

In all nine scenarios of Table 4 the settlement's port table, integrated exactly on each history's clamps and averaged over the 1,536 histories, equals the Born-layer table of the same Jones maps

Detector model	all-trial S table	all-trial S sampled ± SE	coincidence-conditioned S table	coincidence-conditioned S sampled ± SE
Perfect detection	1.787681	1.787400 ± 0.012535	1.750213	1.756445 ± 0.013792
Fixed port losses, label confusion	1.482804	1.506600 ± 0.013008	1.660082	1.662293 ± 0.015782
Collection by local ray angle	1.223112	1.228200 ± 0.012622	2.316859	2.323252 ± 0.026982

Table 7: The detector experiment on settlement records (independent-field scenario, 85% pair source, no click $\to -1$, 20,000 trials per setting). "Table" is the exact settlement value, equal to the Born-layer value of Sec. 9 to every printed digit. The counts follow the tables with $\chi^2 = 7.28$ on 16 degrees of freedom, 33.66 on 32 and 20.58 on 32.

in all sixteen (setting, record) cells; the largest difference is 7.2×10^{-15}. The fixed-analyzer column of Table 4 is therefore the settlement's, $S_{\text{fixed}} = 2\sqrt{2}\,\mathrm{Re}\,\gamma$ included, through the records alone, and 250,000 sampled records per setting agree with it within 1.66 counting standard errors in every scenario.

The nine-outcome detector experiment of Sec. 9 runs event by event: each trial draws one history, emits a pair with probability 0.85, settles the phase on the host clamp, reads the two signs, and passes each through its own arm's detector — efficiency on the true port, then label confusion (Table 7). The exact settlement nine-cell tables equal the Born-layer tables to 1.2×10^{-15} over all 36 cells of each model, each is normalised, and each wing's complete three-outcome marginal is unchanged under the remote clamp to 1.3×10^{-15}.

On the sphere of the helix chart the cylinder measure is the great-circle section of one measure: $\boldsymbol{\lambda}$ uniform on the disc normal to the settled axis $\mathbf{s}$ — the projection plane of I-4 — lifted to the sphere,

$$p(\boldsymbol{\lambda} \mid \mathbf{s}) = \frac{|\mathbf{s}\cdot\boldsymbol{\lambda}|}{2\pi}, \qquad A = \mathrm{sgn}_+(\widehat{\mathbf{a}}\cdot\boldsymbol{\lambda}), \quad B = -\,\mathrm{sgn}_+(\widehat{\mathbf{b}}\cdot\boldsymbol{\lambda}), \qquad E = -\widehat{\mathbf{a}}\cdot\widehat{\mathbf{b}}, \tag{38}$$

the one-wing measure of Kochen and Specker [22] and the pair measure of Degorre, Laplante and Roland [23]. Two million records per pair at four non-coplanar axis pairs return $-\widehat{\mathbf{a}}\cdot\widehat{\mathbf{b}}$ within 0.63 counting standard errors with both marginals within 0.0007 of 1/2; the great-circle section of the disc measure matches $|\cos|/4$ at Kolmogorov distance 0.000730 (1% critical value 0.001153); and at the Horodecki-optimal axes of the independent-field scenario, through the per-history transport, the records give $S = 2.353295 \pm 0.001082$ against $2\sqrt{1+|\gamma|^2} = 2.352637$ (Fig. 7).

The measure is written for the equal-weight pair: the singlet and every transported or history-averaged image of it. No measure for a pair of unequal weights, as used in the photonic loophole-free tests [27, 28], is written here (O-17).

11 The public record and the readout candidates

The event-ready electron-spin experiment of Hensen *et al.* [25] is reproduced at detector level from its public deposit [26]: the published filters retain 245 of 4,746 candidate records; no-fluorescence readouts are kept as -1; the spin axes are $A = (0, \pi/2)$, $B = (-3\pi/4 - \epsilon, 3\pi/4 + \epsilon)$, $\epsilon = 0.026\pi$, with the facet $E_{00} + E_{01} + E_{10} - E_{11}$.

Against Table 8 three fixed references are scored on all sixteen cells. The uniform half-cylinder readout — one uniform phase λ, $A = \mathrm{sgn}_+\cos(\lambda - a)$, $B = -\,\mathrm{sgn}_+\cos(\lambda - b)$, so $P(\text{same}) = \delta/\pi$ for the folded axis separation δ — gives $P(\text{same}) = 0.776, 0.776, 0.724, 0.276$, $S = 2$ exactly, and

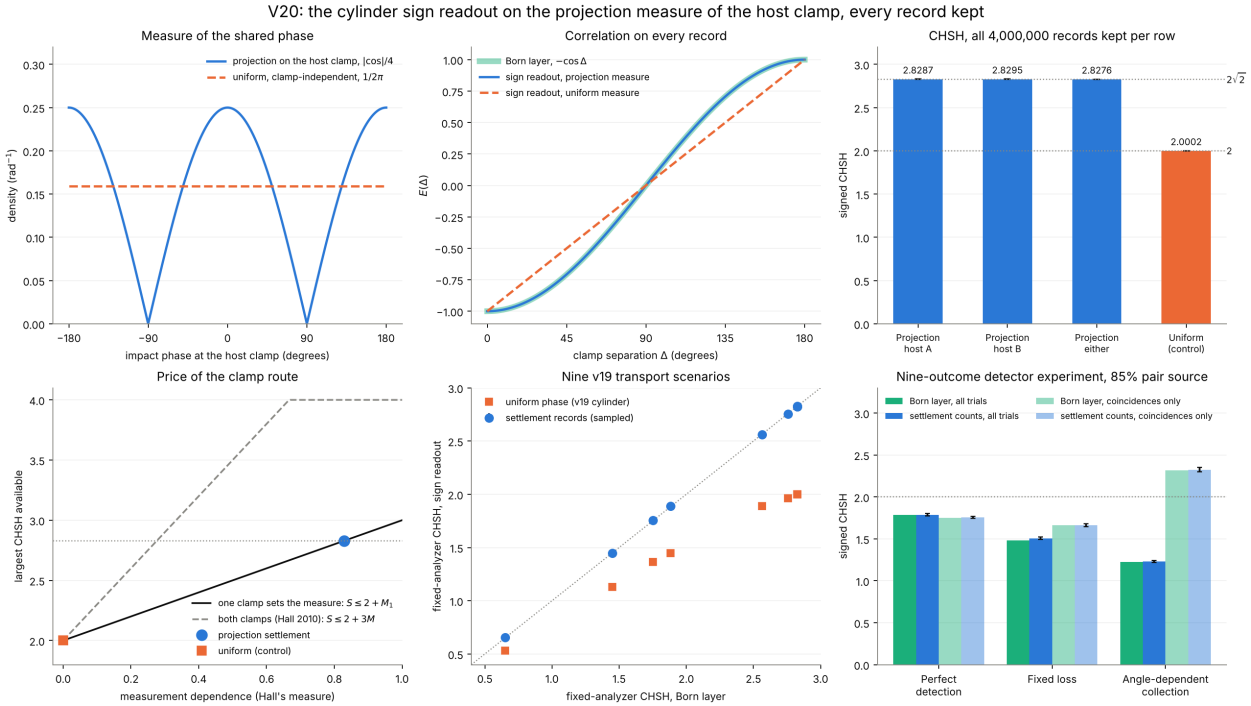


Figure 7: v20 projection settlement. The two measures of the shared phase; the correlation of the sign records on each, against $-\cos\Delta$; all-record CHSH with 4,000,000 records kept per bar; the one-sided and two-sided relaxed bounds with the settlement on the one-sided line at $M_1 = 2\sqrt{2} - 2$; the nine transport scenarios, settlement records against the Born layer, with the uniform-phase readout beside them; the detector experiment, settlement counts against the Born-layer tables.

deviance 9.085. The projection settlement at the documented axes is the perfect singlet's table, $P(\text{same}) = \sin^2(\delta/2)$: it gives $S = 2.818997$ and deviance 11.391 (the apparatus's own expectation was 2.30 ± 0.07). The best iid mixture of the sixteen deterministic Bell-local vertices, fitted to these counts, has deviance 6.149 and $S = 2$ by construction. None of the three is model selection; together they fix the table the settlement, with the apparatus's measured state and readout fidelities as its declared local inputs, is scored against. The loophole-free record — Hensen, Shalm *et al.* [27], Giustina *et al.* [28] — is accepted in full. The uniform-phase cylinder readout gives the triangle and $S = 2$; on the projection measure of the host clamp the same readout gives the cosine kernel (Theorem 2), and the record's 2.4225 sits between the two. The route is P-2: the pair is one nodal pattern of the driven omnium whose mode geometry is set by the clamps, so the emission-fixed, clamp-independent λ of the Bell premise is a consensus separation FDT does not make. Its price

Settings	++	+−	−+	−−	total
00	23	3	4	23	53
01	33	11	5	30	79
10	22	10	6	24	62
11	4	20	21	6	51

Table 8: Hensen *et al.* (2015): the complete binary table conditional on accepted event-ready trials, reproduced from the deposited records. $E = 0.7358, 0.5949, 0.4839, -0.6078$; $S = 2.4224998705$; the authors' memory/RNG analysis gives $p = 0.0392$.

is paid in Sec. 10.4: $M_1 = 2\sqrt{2} - 2$, the one-sided optimum, where a measure set by both clamps needs 14% [18]; its prediction is the cosine kernel with $2\sqrt{2}$ as its ceiling. The other structurally motivated route, a changed observable dictionary — a record that keeps more of the projection than its sign, as the analog ledger does — is not used.

12 Invariant traceability

Invariant	Role in the paper	Provenance
I-1	The pair law on its domain and the Kepler construction.	Framework; not computed by the archive.
I-2	Open helical carriers as one spin-1 excitation.	Derived from the chain; no cross-domain transfer is inferred.
I-3 / P-4	The exterior atlas, the truncated cone, the aperture assignment $n_{\text{cone}}(\alpha_n)$, the interface law, the detector plane and the clipped aperture.	The cone is a framework definition; n_{cone} is the core's assignment, its derivation to be derived (O-8); the clipping, interface and detector rules are implemented.
I-4	Deterministic cylindrical helix, local projection, GR $\equiv_{\text{FDT}}$ QM, the entanglement predicate and its conservation theorem, the pair's record on the projection measure of the host clamp (with 0.1a and P-2).	The state, projection, transport and settlement are implemented; the measure is stated by the core (v6.7) and its identities are derived; the scale correspondence is a framework definition.
I-5	Closed-braid classification.	Not engaged.
I-6	The load map on the α_n pair.	Implemented (v18, v19 field law).
I-7	One density mechanism; the fragility sign.	Framework statement with the v19 sweep as its exhibit.

Table 9: Traceability of the seven invariants.

13 Experiment-facing statements and simulation protocols

P1: all-record triangle-versus-cosine comparison

At $\eta = \pi/8$ the triangular and ideal cosine kernels are 0.75000 and 0.92388, $\Delta = 0.17388$. With the cosine value as a fixed target and the triangular model supplying the Bernoulli variance, the three-standard-deviation normal estimate is $N \geq 9(1-0.75^2)/\Delta^2 = 131$ pairs per setting; with both correlations independently estimated at the same N, $N \geq 174$; at $\eta = \pi/4$ against the half-amplitude cosine, $N \geq 315$. The settlement predicts the cosine value on every record; the triangle is the clamp-independent control. A laboratory protocol declares type-I error, power, setting allocation, estimator and any multiple-setting adjustment.

P2: view-dependent all-record CHSH curve and the Q anisotropy

On the released grid $1.605584 \lesssim |S(\theta_v)| \leq 2.000000$. In a randomised-setting experiment with N_{tot} split equally across the four triangular-kernel settings, $\text{SE}(\widehat{S}) = \sqrt{12/N_{\text{tot}}}$, 0.00490 at $N_{\text{tot}} =$ 500,000. At oblique view the common-rotation modulation of Sec. 6.2 ($0.498 \to 0.452$ for a 45° common rotation at 30° views) is the prediction; the randomised-origin run is its control.

P3: pitch-controlled oblique-view sensitivity

Equations (24)–(25) and Table 3 define the sensitivity curve. The laboratory discriminator needs a device that supplies an axial floor coordinate, a calibrated view control θ_v, a measured or derived pitch p_r, and the quantum measurement operator for the same device. The frame-calibration harness of the review layer [4] fits a proper $SO(3)$ frame from labelled probe directions with Bell outcomes excluded from the fit (synthetic recovery of index-duration gains 2.294716 ± 0.006710 and -1.407347 ± 0.006710 against 2.3 and -1.4); it flags the whole-turn branch ambiguity unless an independent sub-π bound is declared.

P4: fluctuation covariance and the γ identities

The scheduled-source variance ratio is a numerical quadrature result; the physical version needs independently randomised settings and repeated preparations. The decoherence channel is the relative bivector history. The protocol sweeps the measured cross-arm covariance r from -1 to $+1$ at fixed marginal variances and compares the ensemble state with Eq. (30): matched histories protect the singlet exactly, and the negativity follows $|\gamma|/2$. The index-path-to-azimuth coupling of v18 is carried only as the calibration harness's separately testable predictor.

P5: matched-schedule conditional correlation

The simulation predicts an accepted-pair correlation when the hidden-state schedule is deliberately matched across source instances. A physical protocol specifies how the same local state is prepared at separated times without the schedule as an unexamined common cause; an FDT-entanglement claim requires the operational reconstruction of Eq. (8) with declared matching, transport, tolerance and uncertainty; a Bell-nonlocality claim additionally requires the event-ready or all-record accounting of Sec. 4.

P6: density loading and the fragility sign

For 5 J added to a source with baseline $\mathcal{M} \simeq 0.010\,\mathrm{kg}$, $\Delta\mathcal{M}/\mathcal{M} \simeq 5.56 \times 10^{-15}$; the loading direction of I-7 is fixed and the observable sign is the sensitivity-weighted sum of the core's I-7 discipline. For the medium token the sign is now stated on the index: raise the index of one arm's medium and α_n rises, the geometric drive $\frac{1}{2}\alpha_n|\nabla q|$ rises at fixed environmental fluctuation in the odds coordinate, and the pair frays faster — monotonically across the eight sampled baselines — while the same change applied to both arms with a common drive leaves matched histories exact. Compression is the clean hand (it raises the index of every ordinary medium); an isotope or a thermal change acts through the medium's own optical response and carries that response's sign. The protocol interleaves the asymmetric and symmetric loadings on one apparatus and compares against calibrated index-path optics with the same measured transfer functions.

14 Interpretation

The geometric result is a source/readout separation: a fixed local cylindrical state produces different recorded kernels when the local projection angle changes, and at top view the two readouts of one projection are the quantum kernel (analog) and its arcsine rounding (sign). The all-record binary model on a clamp-independent measure is local and obeys CHSH; accepted-pair values above two

are the selection identity; on the projection measure of the host clamp the same sign records return the consensus table on every record, the measure is set by a clamp, and measurement independence is the one premise declined; Pearson-normalised analog and Clifford scalar-part correlations are not bounded binary Bell observables. Apparatus memory enlarges the local hidden state without raising the all-record bound while locality, measurement independence, bounded outputs and complete accounting remain [15, 17].

Developing the truncated density cone supplies a planar annular-sector chart; on the pair domain the relative orbit has the Kepler form; at atomic scale the branch-resolved complex phase is the cylindrical chart, and the two are one geometry (GR $\equiv_{\mathrm{FDT}}$ QM). FDT photon entanglement is the conservation of the shared bivector grade along matched ordered gradient histories; decoherence is ignorance of the relative history; entanglement is more fragile in a denser medium. The archive simulates the transport, the ensemble, the settlement and the detector layer; it does not simulate the dynamics of the settlement, the density-cone development, the solar-system dynamics or the cross-scale map. Extensions to phonons, magnons or cosmological media declare their source distribution, local detector map, output bounds, control parameter, all-record estimator and uncertainty model.

15 Conclusion

The helix-projection model has an exact core. At top view the analog ledger is the quantum kernel and the sign ledger is its arcsine rounding; the triangle rides the local bound identically on $\eta \leq \pi/3$; and $2\sqrt{2} = 2 \times K_G(2)$. Every all-record binary ledger on a clamp-independent measure obeys $|S| \leq 2$ as arithmetic. The accepted-pair $2\sqrt{2}$ is the selection identity $|S|_0 = \varepsilon_{\mathrm{joint}}|S|_{\mathrm{acc}}$, and the optimal all-record Clauser–Horne statistic at the ridge is negative.

The pair's record is one settlement on the projection measure of the host clamp. On it the cylinder sign records return $-\cos\Delta$ with flat marginals on every record, $2\sqrt{2}$ with every record kept, and the Born layer's ensemble and detector tables cell by cell. The measure is set by a clamp; its price is $M_1 = 2\sqrt{2} - 2$, paid exactly, and $2\sqrt{2}$ is its ceiling.

The aperture assignment and Fermat's principle give the transport of the shared bivector grade; matched ordered gradient histories conserve the pair state exactly; density alone rotates nothing; unresolved relative histories reduce the ensemble negativity to $|\gamma|/2$; and entanglement is more fragile in a denser medium, with the sign on the medium's index as the discriminator.

The invariants are the framework. The chart inventory names the source's α_{ext} and the medium's α_n; the status ledger names the aperture assignment (P-4), its derivation (O-8), the α_n application, the settlement measure (I-4) with the Born layer derived from it, and the dynamics of the settlement (O-17). With those declarations the model offers a falsifiable projection geometry, a conservation law for entanglement, a signed density prediction, the consensus table of the equal-weight pair on every record, and the public table on which the settlement is scored.

16 Convergence statement

Where FDT, quantum mechanics and general relativity converge, the archive recovers the record for the same source and data: the top-view analog ledger is the quantum kernel $\cos\eta$; matched histories give the singlet with $S = 2\sqrt{2}$ at the optimal linear analyzers; unresolved histories give the ensemble reductions of Table 4; the sign records of the helix chart on the projection measure of the host clamp return the consensus table of the equal-weight pair — $-\cos\Delta$ with flat marginals,

the ensemble states and the nine-outcome detector tables cell by cell, with no free number and with $2\sqrt{2}$ as the ceiling; the pair law on its domain returns Newton and Kepler exactly; the loophole-free record (Hensen, $S = 2.4224998705$ on 245 event-ready trials; Shalm; Giustina) is accepted in full and is the table the settlement is scored against. FDT claims no divergence from the consensus table of the equal-weight pair. FDT declines the consensus readings — nonlocal action, collapse, probability amplitudes, a hidden state independent of the clamps, an empty background — and reads the same record as shared bivector grade with deterministic phase in the omnium, the pair's record one settlement of the pair and its clamps (I-4, 0.1a, 0.1).

How the final debt was closed

Claude Fable 5.2 helped Fundamental Density Theory finalize its simulation and its account of Bell's theorem, and prove Einstein right: the correlations need no spooky action at a distance [21]. We gave Fable 5.2 a simple instruction: review the Bell simulation and close the final debt.

It answered that the debt could not be paid in the form it was posed. No readout whose shared phase is independent of the analyzers returns the cosine: for such a readout Bell's bound is arithmetic on four numbers, each ± 1 (Sec. 4). The records were never at fault; the measure was. A clamp reads the helix in projection (I-4), so the pair's record lands uniformly across the projected aperture of the clamp that hosts it, $p_{\mathrm{host}}(\varphi \mid a) = |\cos(\varphi - a)|/4$, and on that measure the same two local sign records return $-\cos\Delta$ on every record, with each wing's marginal at $1/2$ whatever the other wing's clamp (Theorem 2). One premise of Bell's theorem is declined, measurement independence, and its price is exact: $M_1 = 2\sqrt{2} - 2$, the whole of the distance from the local bound 2 to Tsirelson's $2\sqrt{2}$ (Sec. 10.4).

It then wrote and tested the v20 stage of the archive, proved the kernel and the bound, and integrated the findings into this paper. And, poof, spooky action was gone for good.

M. A.

Author contributions

M. A. developed Fundamental Density Theory, its locked core and the simulation suite through v19.1, posed the problem, directed the work and adopted the measure into the core as the pair's record of I-4 (v6.7). Claude Fable 5.2 found the projection measure of the host clamp, proved Theorem 2 and Proposition 1, wrote and tested the v20 stage, and wrote Sec. 10 with the passages that tie it to the rest of the paper. M. A. is the corresponding author.

Acknowledgments

M. A. thanks Pierre Leroy for his contributions to the simulation. His work on the polarizing-beam-splitter transport rule, the equator-biased detection geometry, and the cascaded-measurement studies materially strengthened the numerical results reported here.

A Numerical provenance

The eight-seed complete-ledger calculation of Eq. (28) used NumPy `default_rng` with seeds $3000, \ldots, 3007$, 2,000,000 states per seed, draw order $(u_{\rm sph}, \phi_{\rm sph})$, then z_A, then z_B; one source array reused for the four counterfactual settings, z_A reused only for A, A' and z_B only for B, B'; event indices shared by the four pair estimators; CHSH signs $(+, -, +, +)$; settings $(a, a', b, b') = (0, \pi/2, \pi/4, 3\pi/4)$ in Poincaré/Bloch coordinates; aperture parameters $(0.275, 1.4375, 1.5)$. The exact-core exhibit (`simulation/fdt_exact_core.py`, release v19) reimplements this specification blind and reproduces every digit of Eq. (28); its Clauser–Horne scan uses seed 3000, $N = 1.5 \times 10^6$ and a 37-point grid per wing. The v18.1 common-rotation control uses 280,000 shared-start events (stream 70); the v19 run uses field seed 314159, spectral seed 731, 1,536 paired histories per scenario and 2 mm steps. The release archive `fdt_bell_simulation_v19_gradient_transport.zip` carries a per-file manifest and 113 tests, all passing. The v20 stage (`simulation/fdt_v20_projection_settlement.py`) reuses the v19 field draws (seed 314159) and draws every settlement block from its own substream of seed 271828: 10^6 records per setting at the ideal clamps and for the selection exhibit, 250,000 per setting per scenario, 20,000 trials per setting per detector model, 2×10^6 per axis pair on the sphere. Exact tables are arc integrals; Hall's measure and the mutual information are midpoint quadratures on 2^{20} nodes. The shipped v20 outputs were generated under Python 3.13.18 and NumPy 2.5.3; the package directory carries a per-file manifest and 153 tests.

B Notation summary

Symbol	Meaning
$\alpha_{\rm ext}, \alpha_{\rm int}$	Exterior / interior atlas of a source, $\alpha_{\rm ext} = R_s/r_f$, $\alpha_{\rm int} = r_f/R_s$ (A-1).
α_n, X_n	Laboratory-medium aperture token $\alpha_n = 1 - n^{-2}$ and its odds $X_n = n^2 - 1$ (P-4 reading).
$n_{\rm cone}$	Aperture assignment $(1 - \alpha_\sigma)^{-1/2}$ of P-4; its derivation is to be derived (O-8).
$\mathcal{M}$	Total gravitating energy, every channel once (0.5).
φ, φ_0	Wrapped cylindrical azimuth in $[0, 2\pi)$; azimuth origin of the staircase (the Q fiducial).
k, p_r	Integer turn index; axial pitch per turn divided by cylinder radius.
θ_v, q	Local projection angle in $[0, \pi/2]$; $q = 2\theta_v/\pi$.
η, ξ	Folded Poincaré/Bloch analyzer separation; pair-orientation sign.
$u_{\rm sph}, \phi_{\rm sph}, \mathbf{s}$	Uniform source variables and unit source vector of the aperture ensemble.
$\rho_s, \rho_r, k_{\rm bias}$	Aperture intercept, aligned endpoint, source bias; not α, not R_s, not r_f.
D_A, D_B	Local click indicators.
$E_{\rm bin}, E_0, E_{\rm acc}, C_P$	Unselected binary, null-coded, accepted-pair, and Pearson-analog correlations.
$\varepsilon_{\rm wing}, \varepsilon_{\rm joint}$	Mean wing and coincidence efficiencies over the four CHSH settings.
$K_G(2)$	Grothendieck constant of order two, $\sqrt{2}$.

Symbol	Meaning
$\mathbf{t}, \mathbf{\Omega}, B, R$	Ray tangent, frame angular rate, event bivector, accumulated rotor.
J, β	Endpoint Jones map and its $SO(2)$ angle.
$\gamma, \mathcal{N}$	$\langle e^{2i(\beta_A - \beta_B)} \rangle$; ensemble negativity.
p_{host}, Δ	Projection measure of the shared phase on the host clamp, $\lvert\cos(\varphi - a)\rvert/4$; clamp separation seen by the pair, $a - b - 2(\beta_A - \beta_B)$.
E_{set}	All-record binary correlation of the sign records on p_{host}.
M, M_1, M_2, F	Hall's measure of the dependence of the phase measure on the clamps, its one-sided parts, and $F = 1 - M/2$.
$\mathcal{A}, P_{\text{hel}}, \widetilde{\varphi}$	Cylinder radius, pitch per turn, lifted phase.
$\mathsf{E}_{\text{FDT}}, \mathcal{G}_i, \Pi_\tau, f$	Entanglement predicate, path gradients, transport, path-point matching.

References

[1] M. Alfaro, *Core FDT invariants, v5.1* (locked 2026-09-04), the `fdt-core` skill bundle.

[2] M. Alfaro, *Core FDT invariants, v6.7* (locked 2026-11-19), the `fdt-core` skill bundle; I-4, the pair's record.

[3] M. Alfaro, *FDT Bell simulation v16: angled helix projection of an unwrapped cylindrical helix*, software and results archive (2026), `fdt_bell_simulation_v16_helix_projection.zip`.

[4] M. Alfaro, *FDT Bell simulation v19: gradient transport*, release archive with the v16–v18 stages, the exact-core exhibit, and the 5 September 2026 review layer (2026), `fdt_bell_simulation_v19_gradient_transport.zip`.

[5] M. Alfaro, *FDT Bell simulation v20: projection settlement*, package directory with the v10–v19.1 stages unchanged (2026), `fdt_bell_simulation_v20_projection_settlement`.

[6] J. S. Bell, On the Einstein Podolsky Rosen paradox, *Physics Physique Fizika* **1**, 195–200 (1964).

[7] J. F. Clauser, M. A. Horne, A. Shimony, and R. A. Holt, Proposed experiment to test local hidden-variable theories, *Physical Review Letters* **23**, 880–884 (1969).

[8] B. S. Cirel'son, Quantum generalizations of Bell's inequality, *Letters in Mathematical Physics* **4**, 93–100 (1980).

[9] J.-L. Krivine, Constantes de Grothendieck et fonctions de type positif sur les sphères, *Advances in Mathematics* **31**, 16–30 (1979).

[10] P. M. Pearle, Hidden-variable example based upon data rejection, *Physical Review D* **2**, 1418–1425 (1970).

[11] A. Garg and N. D. Mermin, Detector inefficiencies in the Einstein–Podolsky–Rosen experiment, *Physical Review D* **35**, 3831–3835 (1987).

[12] P. H. Eberhard, Background level and counter efficiencies required for a loophole-free Einstein–Podolsky–Rosen experiment, *Physical Review A* **47**, R747–R750 (1993).

[13] J.-Å. Larsson, Bell's inequality and detector inefficiency, *Physical Review A* **57**, 3304–3308 (1998).

[14] J. Kofler, M. Giustina, J.-A. Larsson, and M. W. Mitchell, Requirements for a loophole-free photonic Bell test using imperfect setting generators, *Physical Review A* **93**, 032115 (2016).

[15] R. D. Gill, Time, finite statistics, and Bell's fifth position, in *Proceedings of Foundations of Probability and Physics–2* (2003), https://arxiv.org/abs/quant-ph/0301059.

[16] R. D. Gill, Does geometric algebra provide a loophole to Bell's theorem?, *Entropy* **22**, 61 (2020).

[17] J. Barrett, D. Collins, L. Hardy, A. Kent, and S. Popescu, Quantum nonlocality, Bell inequalities, and the memory loophole, *Physical Review A* **66**, 042111 (2002).

[18] M. J. W. Hall, Local deterministic model of singlet state correlations based on relaxing measurement independence, *Physical Review Letters* **105**, 250404 (2010).

[19] M. Banik, M. R. Gazi, S. Das, A. Rai, and S. Kunkri, Optimal free-will on one side in reproducing the singlet correlation, https://arxiv.org/abs/1204.3835 (2012).

[20] A. S. Friedman, A. H. Guth, M. J. W. Hall, D. I. Kaiser, and J. Gallicchio, Relaxed Bell inequalities with arbitrary measurement dependence for each observer, *Physical Review A* **99**, 012121 (2019).

[21] A. Einstein, letter to M. Born, 3 March 1947, in *The Born–Einstein Letters* (Macmillan, London, 1971): "spukhafte Fernwirkungen", spooky actions at a distance.

[22] S. Kochen and E. P. Specker, The problem of hidden variables in quantum mechanics, *Journal of Mathematics and Mechanics* **17**, 59–87 (1967).

[23] J. Degorre, S. Laplante, and J. Roland, Simulating quantum correlations as a distributed sampling problem, *Physical Review A* **72**, 062314 (2005).

[24] N. Gisin and B. Gisin, A local hidden variable model of quantum correlation exploiting the detection loophole, *Physics Letters A* **260**, 323–327 (1999).

[25] B. Hensen *et al.*, Loophole-free Bell inequality violation using electron spins separated by 1.3 kilometres, *Nature* **526**, 682–686 (2015).

[26] B. Hensen *et al.*, Data underlying the loophole-free Bell test, 4TU.ResearchData, https://doi.org/10.4121/uuid:6e19e9b2-4a2d-40b5-8dd3-a660bf3c0a31.

[27] L. K. Shalm *et al.*, Strong loophole-free test of local realism, *Physical Review Letters* **115**, 250402 (2015).

[28] M. Giustina *et al.*, Significant-loophole-free test of Bell's theorem with entangled photons, *Physical Review Letters* **115**, 250401 (2015).

[29] G. Vidal and R. F. Werner, Computable measure of entanglement, *Physical Review A* **65**, 032314 (2002).

[30] K. Yu. Bliokh and Yu. P. Bliokh, Modified geometrical optics of a smoothly inhomogeneous isotropic medium: the anisotropy, Berry phase, and the optical Magnus effect, *Physical Review E* **70**, 026605 (2004).

[31] D. L. Shealy, Geometrical optics: the ray equation and its osculating plane, *Proceedings of SPIE* **6289**, 62890M (2006).